



**HAL**  
open science

# Exploring the interaction between phase separation and turbulent fluid dynamics in multi-species supercritical jets using a tabulated real-fluid model

Sajad Jafari, Hesham Gaballa, Chaouki Habchi, Jean-Charles de Hemptinne,  
Pascal Mougin

► **To cite this version:**

Sajad Jafari, Hesham Gaballa, Chaouki Habchi, Jean-Charles de Hemptinne, Pascal Mougin. Exploring the interaction between phase separation and turbulent fluid dynamics in multi-species supercritical jets using a tabulated real-fluid model. 2021. hal-03664063

**HAL Id: hal-03664063**

**<https://ifp.hal.science/hal-03664063>**

Preprint submitted on 10 May 2022

**HAL** is a multi-disciplinary open access archive for the deposit and dissemination of scientific research documents, whether they are published or not. The documents may come from teaching and research institutions in France or abroad, or from public or private research centers.

L'archive ouverte pluridisciplinaire **HAL**, est destinée au dépôt et à la diffusion de documents scientifiques de niveau recherche, publiés ou non, émanant des établissements d'enseignement et de recherche français ou étrangers, des laboratoires publics ou privés.

# Exploring the interaction between phase separation and turbulent fluid dynamics in multi-species supercritical jets using a tabulated real-fluid model

SAJAD JAFARI<sup>1</sup>, HESHAM GABALLA<sup>1</sup>, CHAOUKI HABCHI<sup>1</sup>,  
JEAN-CHARLES DE HEMPTINNE<sup>1</sup>, PASCAL MOUGIN<sup>1</sup>

<sup>1</sup>IFP Energies nouvelles, Institut Carnot IFPEN Transports Energie, 1 et 4 avenue de Bois-Préau, 92852 Rueil-Malmaison, France

\*sajad.jafari@ifpen.fr, chaouki.habchi@ifpen.fr

## 1. Abstract

Today, injection of liquid fuels at supercritical pressures is a frequently used technique to improve the efficiency of energy systems and address environmental constraints. This paper focuses on the analysis of the coupling between the hydrodynamics and thermodynamics of multi-species supercritical jets. Various phase transition phenomena, such as droplet formation process by condensation, which have been shown experimentally to significantly affect the flow and mixing dynamics of the jet, are studied. For this purpose, a tabulated multicomponent real fluid model assuming vapor-liquid equilibrium is proposed for the simulation of turbulent n-hexane jets injected with different inflow temperatures (480 K, 560 K, 600 K) into supercritical nitrogen at 5 MPa and 293 K. Numerical results are compared with available experimental data but also with published numerical studies, showing a good agreement. In addition, comparisons between different turbulence models, including the LES Sigma, Smagorinsky and RANS  $K - \epsilon$  models have been performed, showing the relevance of the LES Sigma model for these very complex two-phase flows.

**Keywords:** Real fluid model; Vapor-liquid equilibrium; Tabulation; Multicomponent; Large-eddy simulation; Condensation; Droplet formation process.

## 2. Introduction

In modern high-performance engines, the operating pressures now approach or exceed the critical pressures of the working fluids to increase the engine's efficiency and reduce  $CO_2$  emissions. However, the injection is such that the propellant may enter the chamber at subcritical (cryogenic temperature) or supercritical temperature, corresponding to liquid-like (LL) or gas-like (GL) states, respectively [1–3]. The properties in these states significantly deviate from the ideal gas as they introduce some thermodynamics' non-idealities and transports anomalies. Two-phase flows covering (LL) and (GL) conditions are known in the literature as the transcritical regime [1–9]. At subcritical conditions, the phase transition phenomena are either classified as evaporation or condensation. Generally, it has been accepted that the subcritical liquid-to-gas transition is characterized by a structural change from an ordered (liquid) to a disordered (gas) state. In this case, density can be chosen as the appropriate order parameter, which exhibits a sharp discontinuity when phase transition occurs [10–12]. Besides, pseudo phase transition (i.e. pseudo-boiling or pseudo-condensation) may occur in the supercritical state at the crossover between LL and GL fluids, where the density changes sharply but continuously. The locus where this sharp transition from LL and GL fluids is currently not well understood. The Widom line [3, 8, 10, 11], defined as the heat capacity maximum, is usually used to separate the LL and

43 GL supercritical fluids. However, the Widom line cannot be clearly defined at high pressure  
 44 and high temperature (see Figure 1(b)), where the minima of the thermal diffusivity coefficients  
 45 are found to be more appropriate by Gorelli et al. [12] for tracking the transition between the  
 46 supercritical LL and GL fluids. In the pseudo-boiling transition, no structural change has been  
 47 observed in macroscopic light scattering experiments [6, 7]. As such, these phenomena share a  
 48 nonlinear behavior similar to that of the subcritical condition when the coexistence line is crossed,  
 49 as illustrated in Figure 1. For pure n-Hexane ( $C_6H_{14}$ ), this figure shows the phase transition  
 50 in subcritical states (i.e., evaporation and condensation processes) when the coexistence line is  
 51 crossed. Also, the gradual phase-change processes in the transcritical regime (i.e., pseudo-boiling  
 52 and pseudo-condensation) as soon as it meets the Widom line. This illustrates that phase  
 53 transition, including bubble or droplet formation process, evaporation, and condensation, are  
 54 mainly driven by changes in pressure or temperature for a single-component fluid.  
 55 As a matter of fact, researcher's interest in the behavior of supercritical fluids dates back to at  
 56 least 1869 [13]. However, despite recent theoretical, experimental, and computational efforts,  
 57 these phenomena are still not fully understood especially for multicomponent systems. In  
 58 the past decades, extensive studies have been performed for understanding the behavior of a  
 59 single-component phase transition [3, 8, 9, 12, 14–18]. One of the pioneering and remarkable  
 60 studies was conducted by Chehroudi et al. [15]. They experimentally studied the jet behavior of  
 61 pure liquid nitrogen injected into gaseous nitrogen at subcritical and supercritical pressures. They  
 62 observed that in subcritical pressures, due to the significant surface tension, the interface between  
 63 the liquid and the gas plays an important role, and it leads to the appearance of the primary and  
 64 secondary breakup, known as classical atomization. However, as the pressure increases, the  
 65 magnitude of the surface tension decreases and vanishes at the critical point, which suppresses the  
 66 formation of ligaments and droplets for supercritical pressures. However, liquid-like ligaments  
 67 (also called finger-like) could be seen in their shadowgraphy experimental results despite the  
 68 absence of surface tension, especially for the transcritical injection regime. Therefore, injection  
 69 above the critical pressure of a single-component propellant can be considered as a diffuse

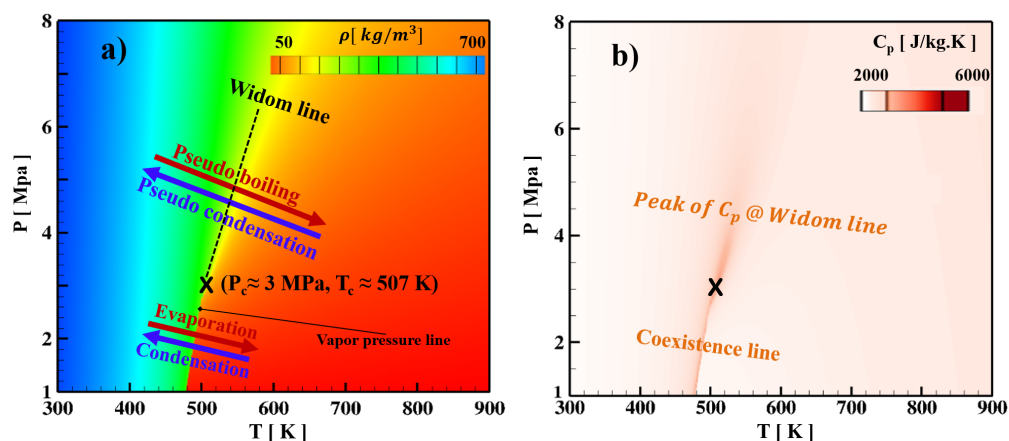


Fig. 1. Illustration of the phase transition in subcritical states (i.e., evaporation and condensation processes) when the coexistence line is crossed, and gradual phase change processes in the transcritical regime (i.e., pseudo-boiling and pseudo-condensation) when crossing the Widom line. Pressure-Temperature diagram: (a) Density contour mapped by coexistence and Widom lines, and (b) Heat capacity contour for  $C_6H_{14}$ . Nonlinear behavior is present along the Widom line but also along the liquid-vapor coexistence line.

70 interface mixing process rather than a classical atomization of the interface. However, the same  
71 is not valid for multicomponent systems for which the local critical pressure of the mixture  
72 could dramatically exceed the value of the pure components. Indeed, various studies have  
73 been carried out for multicomponent systems, and their interfacial phase transition has been  
74 revealed to be more complex than for a single-component system, mainly due to the variation of  
75 the mixture critical point with the local composition of the fluid [8, 17, 19–25]. Furthermore,  
76 this difference in phase transition mechanisms between single and multicomponent systems  
77 leads to various interface structures that influence the jet behavior [1, 8, 21, 22]. Crua et al. [1]  
78 studied the injection of liquid (n-heptane, n-dodecane, n-hexadecane) into supercritical nitrogen  
79 at different temperatures and pressures. They investigated the transition from a two-phase to a  
80 single-phase mixing regime and established a criterion for switching between the two regimes as  
81 a function of the critical temperature and pressure of the pure fuels. However, due to the limited  
82 accuracy of the experimental setup, reliable data are still lacking for the precise identification  
83 of the transition between the two-phase and single-phase mixing regime that could be used for  
84 validating numerical models. In addition, there are still multiple doubts and questions about the  
85 conditions and mechanisms behind the interface disappearance for multicomponent systems.

86 Other interesting experimental studies have recently done by Gerber et al. [6, 7]. These studies  
87 focused in particular, on under-relaxed jets for which a shock waves train was observed in the  
88 near nozzle region. They concluded that high-pressure jets have the same scattering footprint and  
89 morphological properties as low-pressure jets. However, enhanced scattering is only observed  
90 upon multiple crossings of the Widom region, e.g., due to the series of rapid recompressions caused  
91 by the shock train. This enhanced scattering is caused by the enhancement in compressibility  
92 and density fluctuation when the fluid switches between LL and GL. Therefore, the experimental  
93 findings of Gerber et al. [6, 7] show that density fluctuations are not negligible across the Widom  
94 line. They can be detected both at the macroscopic (continuum) and molecular scale. Indeed,  
95 these findings were confirmed at molecular scales by the small-angle X-ray scattering experiments  
96 in [26]. This completely changes the physical meaning of pseudo-boiling/pseudo-condensation  
97 transition from the subcritical counterpart (evaporation/condensation).

98 Another interesting study was recently carried out by Traxinger et al. [21]. They experimentally  
99 and numerically studied a multicomponent system consisting of a high-pressure n-hexane jet at  
100 three different temperatures (480K, 560K, 600K), injected into a chamber filled with supercritical  
101 nitrogen at ( $P = 5MPa$  and  $T = 293K$ ). Specifically, the focus was on the phase separation  
102 of an initially supercritical fluid due to the interaction with its surrounding. Simultaneous  
103 shadowgraphy and elastic light scattering (ELS) experiments were conducted by Traxinger et  
104 al [21] to capture both the flow structure as well as the phase separation. Remarkable results have  
105 been shown experimentally for the case of supercritical n-hexane with  $T=560$  K, exceeding its  
106 critical temperature and pressure, injected into supercritical nitrogen at  $T = 293K$  and  $P = 5MPa$ .  
107 Indeed, the condensation of n-hexane has been observed in these conditions, as expected from  
108 their priory thermodynamic study. The phase transition is initiated in the mixing layer some  
109 distance downstream of the nozzle and eventually mixes with the jet core at large distances. In  
110 addition, at a higher injection temperature of n-hexane ( $T = 600K$ ), this phenomenon of phase  
111 transition does not occur, and the gaseous fuel injected into the chamber gradually mixes with  
112 the ambient gas. Finally, a classical subcritical atomizing n-hexane jet was imaged at the lowest  
113 n-hexane injection temperature ( $T = 480K$ ). The various experimental and numerical results  
114 of Traxinger et al. [21] will be used in the present work to validate our Computational Fluid  
115 Dynamics (CFD) tabulated Real-Fluid Model (RFM) presented in Section 3.

116 Developing a CFD model capable of handling subcritical, transcritical, and supercritical  
117 conditions, including possible phase transition, is crucial to enable a more accurate analysis of  
118 multicomponent systems. To study these complex behaviors, it is therefore essential to use a  
119 real fluid model capable of automatically switching from a single-phase flow to a two-phase

120 flow, and vice versa [8, 17, 21, 24, 25]. However, real fluid simulations have been proven to be  
121 computationally time-consuming. Indeed, it has been found that the complexity of cubic EoS  
122 and solving the Vapor-Liquid-Equilibrium (VLE) iteratively using the isoenergetic-isochoric  
123 (UVn)-flash set of equations are computationally expensive [8, 17, 24, 25, 27–30]. Therefore, an  
124 accurate, robust, and most importantly an efficient real-fluid model is required, which is one  
125 of the main objectives of the presented work. A remedy for this problem is to set up a table  
126 before the start of the simulation and store the values of the required thermodynamic properties  
127 in it. Then, rapid searching, as well as an interpolation, are carried out in the table during the  
128 simulation. This process of searching and interpolation is usually called “a look-up table” in  
129 the literature. More details about tabulation, interpolation, and look-up of data can be found  
130 in [8, 31–36].

131 In summary, in this study, a fully compressible, multicomponent real fluid model accounting  
132 for VLE is proposed using a generalized three-dimensional (3D) tabulation method [8, 30, 31].  
133 The tabulated thermodynamic properties of the binary mixture are calculated as a function  
134 of temperature (T), pressure (P), and mass fraction of the first species in the mixture (Y). In  
135 this model, an in-house thermodynamic library IFPEN-Carnot is used to generate a 3D table  
136 (with T-P-Y as the axis for a binary mixture) based on various real fluid EoS. This IFPEN-  
137 Carnot thermodynamic library includes different EoSs, such as Peng-Robinson (PR-EoS) [37],  
138 Soave–Redlich–Kwong (SRK-EoS) [38], and Cubic Plus Association (CPA-EoS) [39], which also  
139 represents one of its main advantages [8, 40]. For computational speed and robustness, a uniform  
140 look-up table is generated based on an isothermal-isobaric TPn-flash [8, 17, 25, 29]. The RFM  
141 model was implemented together with the generalized 3D tabulation method in CONVERGE  
142 solver [41].

143 This paper is organized as follows. Section 3 is dedicated to the explanation of the numerical  
144 and theoretical methods, including the governing equations, thermodynamic tabulation, and  
145 look-up methods. Section 4 is devoted to understanding the condensation phenomenon during  
146 the supercritical injection of hexane into nitrogen using the proposed RFM model. In addition,  
147 comparisons between various turbulence models, including large-eddy simulations (LES Sigma  
148 [42] and Smagorinsky [43]) models as well as a Reynolds Averaged Navier-Stokes (RANS  
149  $K-\epsilon$ ) [44] model will be carried out and discussed. Subsequently, the numerical results in sections  
150 4 and 5 are compared with available experimental data, but also with published numerical studies.  
151 Finally, this paper is summarized and the conclusions are presented in section 6.

### 152 3. The real-fluid RFM model

153 The real-fluid RFM model [8, 40, 45] used in the current work is presented in this section. It is  
154 a fully compressible model developed under the homogeneous equilibrium modeling (HEM)  
155 assumption, considering multicomponent in both phases. Indeed, the RFM model has been  
156 developed assuming the two-phase system to be under the assumptions of thermodynamic  
157 equilibrium (i.e., equilibrium of the velocity, pressure, temperature, and chemical potential  
158 at liquid-vapor interfaces). This assumption guarantees the required hyperbolic mathematical  
159 formulation for the RFM model. The set of governing equations as employed in the CONVERGE  
160 CFD solver [41] has been used as a base framework for the development of the tabulated RFM  
161 model presented below. More details about this modelling approach could be found in Jafari et  
162 al. [8].

#### 163 3.1. Governing equations of the flow solver

164 The set of governing equations are presented through equations (1 - 4) including the density  
165 transport equation, species transport equation, mixture momentum equation and mixture specific  
166 internal energy equation, respectively.  $(\rho, u_i, P, T, e)$  are the mixture’s density, velocity, pressure,  
167 temperature, and specific internal energy, respectively.  $(Y_m, h_m)$  are mass fraction and enthalpy

168 of species ( $m$ ) in the mixture, respectively.  $N_s$  is the total number of species.

$$\frac{\partial \rho}{\partial t} + \frac{\partial \rho u_i}{\partial x_i} = 0 \quad (1)$$

$$\frac{\partial \rho Y_m}{\partial t} + \frac{\partial \rho Y_m u_j}{\partial x_j} = \frac{\partial}{\partial x_j} (\rho D \frac{\partial Y_m}{\partial x_j}), m = \{1 \dots N_s - 1\} \quad (2)$$

$$\frac{\partial \rho u_i}{\partial t} + \frac{\partial \rho u_i u_j}{\partial x_j} = \frac{\partial P}{\partial x_i} + \frac{\partial \tau_{ij}}{\partial x_j} \quad (3)$$

$$\frac{\partial \rho e}{\partial t} + \frac{\partial \rho e u_j}{\partial x_j} = -P \frac{\partial u_j}{\partial x_j} + \tau_{ij} \frac{\partial u_i}{\partial x_j} + \frac{\partial}{\partial x_j} (\lambda \frac{\partial T}{\partial x_j}) + \frac{\partial}{\partial x_j} (\rho D \sum_m h_m \frac{\partial Y_m}{\partial x_j}) \quad (4)$$

172 where the viscous stress tensor ( $\tau_{ij}$ ) is given by

$$\tau_{ij} = \mu (\frac{\partial u_i}{\partial x_j} + \frac{\partial u_j}{\partial x_i}) - 2/3 \mu (\frac{\partial u_k}{\partial x_k}) \delta_{ij} \quad (5)$$

173  
174 It is worth mention that the calculations of the real fluid thermodynamic properties are performed  
175 based on the residual approach [17, 46]. In this approach, any thermodynamic function is  
176 computed from the sum of an ideal gas part and a residual part. The ideal gas part is determined  
177 from a specific polynomial equation [47]. While the residual part, which represents the deviation  
178 from the ideal gas behavior is deduced from the employed equation of state (EoS). More details can  
179 be found in our previous studies [17, 25]. Besides, the thermal conductivity ( $\lambda$ ) and the dynamic  
180 viscosity ( $\mu$ ) cover laminar and turbulent contributions, as cumulative transport properties of  
181 the fluid. The laminar contribution of ( $\lambda, \mu$ ) is computed by Chung et al. [48] correlations. The  
182 turbulent conductivity is calculated using a given turbulent Prandtl number  $Pr_t$ , as ( $\lambda_t = \frac{C_p \mu_t}{Pr_t}$ ),  
183 where ( $C_p$ ) is the isobaric heat capacity and the turbulent viscosity ( $\mu_t$ ) is computed by the  
184 adopted turbulence model. Also, the laminar, and turbulent diffusion coefficients are estimated  
185 using given laminar and turbulent Schmidt numbers, ( $Sc$ ) for  $D = \mu / (\rho Sc)$ , and ( $Sc_t$ ) for  
186  $D_t = \mu_t / (\rho Sc_t)$ , respectively. In this regard, various turbulence models including large-eddy  
187 simulations (LES Sigma [42] and Smagorinsky [43]) models as well as a Reynolds Averaged  
188 Navier-Stokes (RANS  $K-\epsilon$ ) [44] model have been considered in this study (See Section 4) to  
189 investigate the effect of the turbulence modeling on the numerical results.

### 190 3.2. Numerical schemes

191 The above set of governing equations (1 - 4) of the two-phase RFM model is solved numerically  
192 using a diffuse interface modeling approach (DIM). In the CONVERGE CFD solver, all the  
193 dependent parameters are collocated at the center of the computational cell. To prevent checker-  
194 boarding, the Rhie-Chow algorithm is employed [49]. Besides, a second-order-accurate spatial  
195 discretization scheme, plus a first-order Euler temporal scheme, are used for the governing  
196 conservation equations discretization. The transport equations are solved using a density-based  
197 solver, where an extended Pressure Implicit with Splitting of Operators (PISO) algorithm, method  
198 of Issa [50], has been adapted for real fluid equations of state. More details on the modified PISO  
199 algorithm can be found Jafari et al. [8].

### 200 3.3. Equilibrium thermodynamic closure of the flow solver, and the tabulation look-up

201 For the supercritical jet with ( $C_6H_{14}, N_2$ ) binary mixture, the real-fluid Peng-Robinson (PR) [37]  
202 equation of state (EOS) has been selected for the thermodynamic closure of the RFM model  
203 transport equations (1 - 4). A general form of this cubic EoS can be written as equations (6,7),  
204 along with the various parameters that are listed in Table 1 [37], where index ( $c$ ) stands for

Table 1. Parameters for PR equation of state (index c stands for critical value)

$\delta_1$	$\delta_2$	$(a_c)_i$	$m_i$	$b_i$
$1 + \sqrt{2}$	$1 - \sqrt{2}$	$0.45727 \frac{R^2 T_c^2}{P_c}$	$0.37464 + 1.54226\omega - 0.26992\omega^2$	$0.0778 \frac{RT_c}{P_c}$

205 critical point value for a pure component when it appears as in  $T_c$  or  $P_c$ . Also, it is worth noting  
 206 that local mixture critical point values are denoted by a  $(c, mix)$  index.

$$P = \frac{RT}{v - b} - \frac{a(T)}{(v + \delta_1 b)(v + \delta_2 b)} \quad (6)$$

207

$$a_i(T) = (a_c)_i \left[ 1 + m_i \left( 1 - \sqrt{\frac{T}{T_c}} \right) \right]^2 \quad (7)$$

208 Besides, when the PR-EoS is used for mixtures, van der Waals mixing rules are applied as equation  
 209 (8), where  $(k_{ij})$  is the binary interaction parameter (BIP) that can be fitted to experimental data  
 210 to well represent the phase diagram of a binary system,  $x_i$  is the molar fraction, and  $a_i(T)$  is the  
 211 parameter calculated using Equation (7) for component  $i$ . In this study,  $k_{ij}$  is set to zero.

$$a(T) = \sum_i \sum_j x_i x_j \sqrt{a_i(T) \cdot a_j(T) (1 - k_{ij})} \quad (8)$$

$$b = \sum_i x_i \cdot b_i$$

212

213 Generally, it is well known that cubic EoSs with van der Waals (vdW) mixing rule are not really  
 214 well suited for computing densities [8, 25]. However, our achievement in this study demonstrate  
 215 that the PR EoS [37] can acceptably predict the density and specific heat capacity for n-hexane (a  
 216 relatively light component) at  $P = 5 \text{ MPa}$ , which are in an excellent agreement with the reference  
 data taken from NIST [51], as shown in Figure 2.

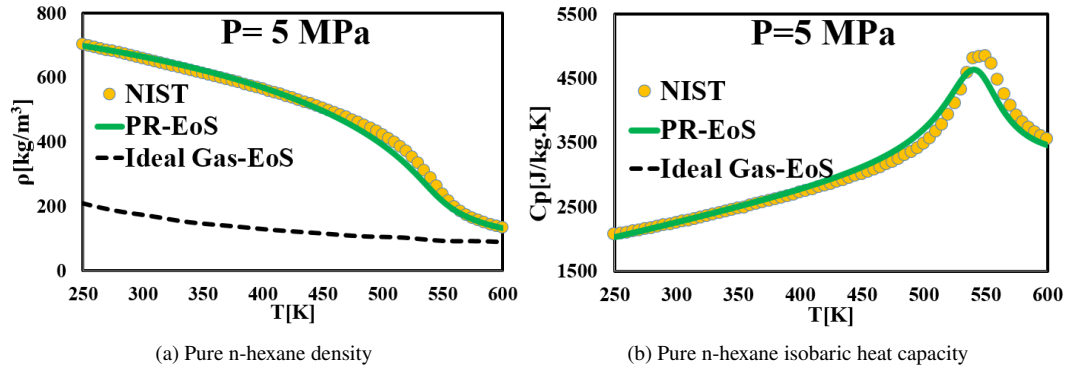


Fig. 2. Comparison of PR-EoS and ideal gas EoS with reference data obtained from NIST [51] for n-hexane at  $P = 5 \text{ MPa}$  showing a) Density, and b) Isobaric heat capacity profiles. The results, using PR-EoS, Peng Robinson equation of state, are in a good agreement with NIST data [51], however the fluid properties specially for isobaric heat capacity (outside the range) significantly differ from an ideal gas at this high pressure  $P = 5 \text{ MPa}$ .

217

218 The current work adopts a tabulation approach, where the thermal and transport properties, as  
 219 well as the phase states and compositions, are tabulated before the CFD simulation. During the  
 220 simulation, the various tabulated properties, such as density, specific internal energy, isobaric heat  
 221 capacity, isochoric heat capacity, viscosity, conductivity, gas volume fraction, and species liquid  
 222 mass fraction in each phase, are linearly interpolated using three inputs, which are temperature  
 223 (T), pressure (P), and species mass fraction in the mixture ( $Y_m$ ,  $m = 1 : N_s - 1$ ), where  $N_s$  is  
 224 the total number of species. As we saw above for the binary systems ( $N_s = 2$ ),  $Y_1$  is subsequently  
 225 denoted  $Y$ , as the third axis of the 3D-Table. In this study, this table is generated based on  
 226 the IFPEN-Carnot thermodynamic library, which uses a robust isothermal-isobaric (TPn)-flash  
 227 algorithm coupled with the PR-EoS. This tabulation approach offers the advantage of avoiding  
 228 the direct evaluation of the non-linear cubic EoS along with the VLE calculation during the  
 229 simulation, which has been proven to be computationally demanding and costly [8, 17, 25, 30, 31].  
 230 Moreover, the tabulation approach based on the IFPEN-Carnot thermodynamic library allows  
 231 simulating different fuels and surrogates without the need of hard coding a (TPn) flash for each  
 232 EoS of interest.

233 With respect to interpolating the data in the table during runtime, the simplistic inverse distance  
 234 weighting (IDW) is implemented [52]. This critical step is mainly carried out during the  
 235 simulation for two main tasks:

236 **1. A Table look-up function:**

237 *Compute the thermal, transport properties as well as the phase state using the input*  
 238 *parameters ( $T, P, Y_m$ ) with  $m = 1 : N_s - 1$ .*

239 **2. A Reverse look-up function:**

240 *Compute/Update the temperature using the inputs ( $e, Y_m, P$ ) once the mixture mass fraction*  
 241 *( $Y_m$ ) and the energy ( $e$ ) transport equations are solved for each pressure ( $P$ ) in the PISO*  
 242 *loop.*

243 A general form of finding an interpolated value of  $u_i$  at a given point  $X$  based on samples  
 244  $u_i = u(X_i)$ ,  $i = 1, \dots, N$  using IDW can be expressed as equation (9), where  $\omega_i(X) = \frac{1}{d(X, X_i)}$ ,  $X$   
 245 denotes an interpolated (arbitrary) point,  $X_i$  is an interpolating (known) point,  $d$  is the given  
 246 distance from the known point  $X_i$  to the unknown point  $X$ ,  $N$  is the total number of known points  
 247 used in each local interpolation.  $N = 8$  for uniform 3D table.

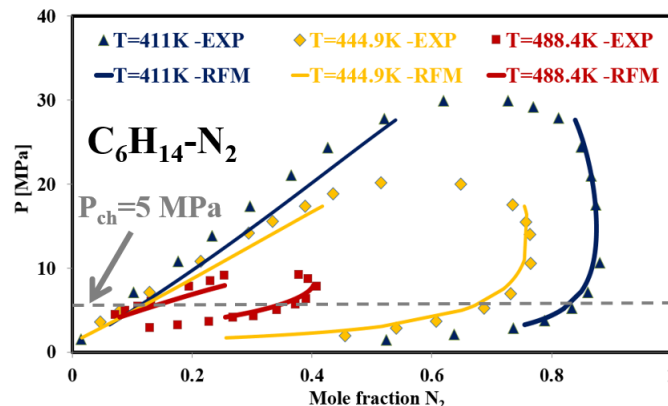


Fig. 3. Vapor-Liquid equilibrium of  $C_6H_{14} - N_2$  calculated in this study using PR-EoS compared to the experimental data [53]

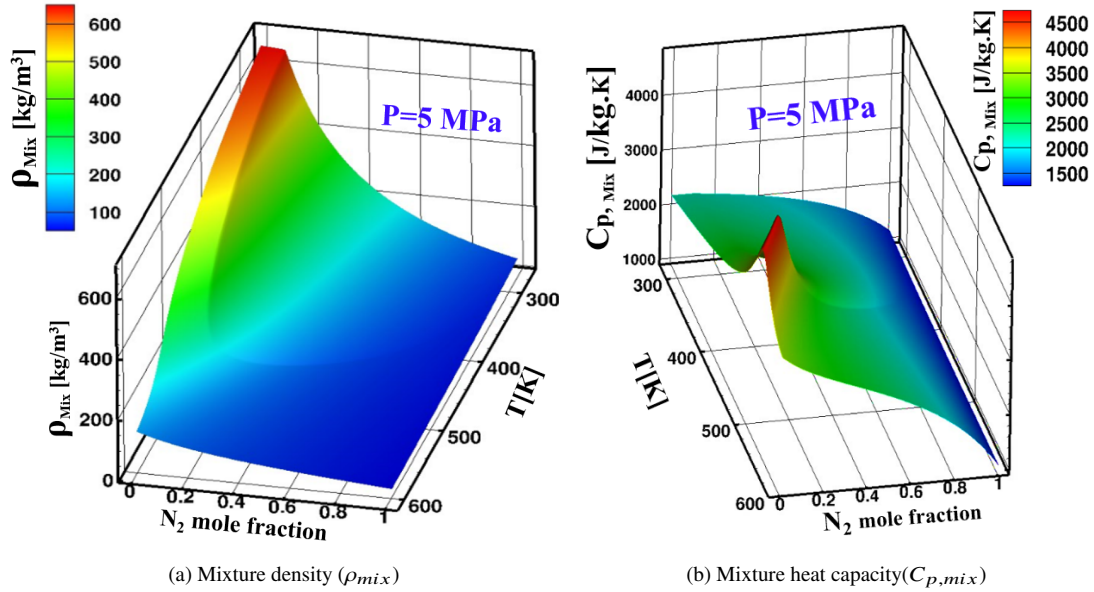


Fig. 4. Contour plots of (a) mixture density, and (b) mixture heat capacity for  $C_6H_{14} - N_2$  at  $P_{ch} = 5 MPa$ . As the plots show, due to the different non-linearity for various properties, the grid independency for having a refined thermodynamic table is mandatory.

248

$$u(X) = \begin{cases} \frac{\sum_{i=1}^N \omega_i(X) u_i}{\sum_{i=1}^N \omega_i(X)} & \text{if } d(X, X_i) \neq 0 \text{ for all } i \\ u_i & \text{if } d(X, X_i) = 0 \text{ for some } i \end{cases} \quad (9)$$

### 249 3.4. Validation of the VLE solver

250 As explained in the introduction, the state properties deviate considerably from those of the ideal gas,  
 251 as they introduce some thermodynamic non-linearity and a transport anomaly at supercritical  
 252 pressures, as shown in Figure 2. Indeed, as it can be seen in Figure 2, compared to the density  
 253 and isobaric heat capacity from NIST [51] for n-hexane at  $P = 5 MPa$ , ideal gas EoS cannot  
 254 predict the transcritical behavior of such properties, ideal gas EoS is outside the range. However,  
 255 more accurate and complex EoS, as PR EoS, can predict the transcritical behavior with a good  
 256 agreement, especially for the isobaric heat capacity.

257 To validate the VLE thermodynamic solver, the VLE for a binary mixture of  $C_6H_{14} - N_2$  using  
 258 PR-EoS has been compared with the available experimental data [53], as shown in Figure 3.  
 259 It can be seen that the calculation results of the VLE solver are in good agreement with the  
 260 experimental data over the entire ranges of pressure for the different temperatures. Furthermore,  
 261 Figure 4(a,b) shows the variation of the mixture density and heat capacity, respectively, for a  
 262 binary mixture of  $C_6H_{14} - N_2$  as a function of temperature and  $N_2$  mole fraction at  $P=5 MPa$ .  
 263 These results have been obtained using a uniform table with  $\Delta T = 1K$ ,  $\Delta Y_{N_2} = 0.005$  in grid  
 264 sizes on the axis. Due to the different non-linearity of the properties shown in Figure 4(a,b), a  
 265 grid independence for the thermodynamic table is mandatory, which should correctly capture  
 266 various interesting phenomena such as the heat capacity peak ( $C_{p,mix}$ ) around the Widom line  
 267 for certain compositions of this multi-species system, see Figure 4(b). It is worth mentioning that  
 268 the values of properties in two-phase region, in the vapor liquid equilibrium dome, are computed

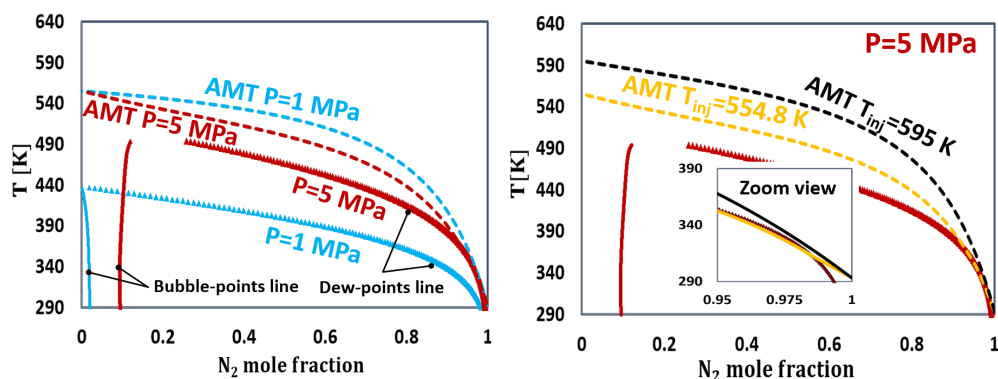
269 from the mixing of the liquid and vapor phase properties using the vapor fraction, more can be  
 270 found here [8, 17].

### 271 3.5. Analytical study of condensing supercritical jet

272 This section focuses on the analysis of the thermodynamic states of a condensing supercritical jet.  
 273 As reported in the introduction, condensation of n-hexane has been recently shown experimentally  
 274 by Traxinger et al. [21] when it is injected in supercritical state at  $T_{inj} = 560K$  into a supercritical  
 275 nitrogen at  $T_{ch} = 293K$  and  $P_{ch} = 5MPa$ . They observed that condensation is initiated in the  
 276 mixing layer and eventually mixes in the core of the jet forming a spray of droplets at great  
 277 distance from the nozzle. In such conditions, the mixture temperature distribution in the chamber  
 278 is usually varying in the range between  $T_{inj} = 560K$  and  $T_{ch} = 293K$ . Indeed, assuming an  
 279 adiabatic process neglecting heat exchange, the enthalpy of the mixture at equilibrium  $H_{mix}$  is  
 280 equal to the weighted molar average of the enthalpy of the pure components,  $H_{N_2}$  and  $H_{C_6H_{14}}$  :

$$281 \quad H_{mix}(T_{AM}, P_{ch}, z_{N_2}) = z_{N_2}H_{N_2}(T_{ch}, P_{ch}) + z_{C_6H_{14}}H_{C_6H_{14}}(T_{inj}, P_{ch}).$$

282 The adiabatic mixture temperature, denoted ( $T_{AM}$ ) is the solution of this equation, as the  
 283 enthalpy values are calculated using PR-EoS using our in-house thermodynamic library.  $z_{N_2}$   
 284 is the mole fraction of  $N_2$  (with  $z_{N_2} + z_{C_6H_{14}} = 1$ ).  $T_{inj}$ ,  $T_{ch}$ ,  $P_{ch}$  denote the temperature of  
 285 the injected n-hexane at the exit of nozzle, the initial temperature of  $N_2$  in the chamber, and  
 286 the initial chamber pressure (here constant and equal to  $5MPa$ ), respectively. More details on  
 287 AMT can be found in [55]. Figure 5(a,b) displays the AMT temperatures (dashed lines) for two  
 288 different chamber pressures at  $P = 1MPa$  and  $P = 5MPa$  in a  $T$ - $x_{N_2}$  phase diagram (triangle)  
 289 obtained using PR-EoS. As shown in Figure 5(a), the AMT, dash lines, are plotted with the same  
 290 inflow temperature,  $T_{inj} = 554.8K$  and chamber temperature,  $T_{ch} = 293K$ . For the low pressure  
 291 case,  $P = 1MPa$ , the AMT does not cross the corresponding two-phase boundary, and hence  
 292 the jet is supposed to stay in the single-phase mixing regime. However, for the higher pressure  
 293 case,  $P = 5MPa$ , the AMT crosses the corresponding two-phase boundary very close to the  $N_2$   
 294 mole fraction of one and it is therefore expected that the jet enters the two-phase region near  
 295 the periphery of the jet as shown experimentally in Traxinger et al. [21]. In addition, it can  
 296 be seen in Figure 5(a) that the slope ( $dT/dx$ ) of the phase diagram (near  $x_{N_2} = 1$ ) can control  
 297 the phase separation process (condensation) and the formation process of spray droplets for  
 298 certain temperature and pressure ranges of the supercritical injection regime. Besides, Figure  
 299 5(b) shows and confirms the same behavior for a constant pressure,  $P = 5MPa$  but at two  
 300 different n-hexane inflow temperatures,  $T_{inj} = 554.8K$ , and  $T_{inj} = 595K$ . Indeed, this figure  
 301 shows that by increasing the inflow temperature to  $595K$ , the AMT no longer crosses the phase  
 302 boundary. Therefore, this theoretical analysis has demonstrated that due to the slope ( $dT/dx$ ) near  
 303  $x_{N_2} = 1$  in the phase diagram, the periphery of a supercritical jet may or may not nucleate and  
 304 condense. This proves that jet structure in a multicomponent system does not follow the same  
 305 behavior as in a single-component jet. In summary, for supercritical jet of  $C_6H_{14}$  injected into  
 306  $N_2$  colder ambient, droplet formation process by condensation are expected to be triggered at  
 307 the jet's periphery when the AMT crosses the two-phase region. Otherwise, the periphery of  
 308 the supercritical jet is going to mix with the ambient gas remaining in the supercritical regime  
 309 without any droplet formation process. This supercritical droplet formation process/condensation  
 310 phenomenon, which has been the subject of some recent studies [21, 22], will be investigated in  
 311 more detail in the next section based on the tabulated RFM model applied in the LES numerical  
 312 framework.



(a) Condensing and non-condensing supercritical regime at different pressures (b) Condensing and non-condensing supercritical regime at different temperatures at  $P=5$  MPa

Fig. 5. Condensing and non-condensing supercritical regime (a) at different pressures, (b) at different temperatures. AMT denotes adiabatic mixing temperature, plotted by dash lines, and by crossing the phase boundary (dew points line), the droplet formation process, and the condensation begins and develops at the periphery of the jet. If the AMT doesn't cross the two-phase dome, it will remain at supercritical regime without any droplet formation process, non-condensing supercritical regime (single phase mixing regime).

## 313 4. Results and discussion

### 314 4.1. Test cases definition

315 This section is devoted to the numerical study of the turbulent jet mixing process of n-hexane  
 316 ( $C_6H_{14}$ ) injected into supercritical nitrogen ( $N_2$ ). More precisely, following the investigations  
 317 of Traxinger et al. [21], n-hexane is injected at three temperatures (480K, 560K, 600K) into a  
 318 chamber initially filled with  $GN_2$  at an ambient pressure of  $P_{ch} = 5MPa$ . The critical pressure  
 319 and temperature of pure  $C_6H_{14}$  and  $N_2$  are ( $P_c \approx 3MPa$ ,  $T_c \approx 507K$ ) and ( $P_c \approx 3.4MPa$ ,  
 320  $T_c \approx 126.2K$ ), respectively. Hence, the ambient pressure,  $5MPa$  correspond to a reduced  
 321 pressure  $P_{r,C_6H_{14}} \approx 1.67$  for pure n-hexane, and  $P_{r,N_2} \approx 1.47$  for pure  $N_2$ . However, due to  
 322 the mixing of two components, the mixture critical point will vary locally as function of the  
 323 mixture composition. Therefore, with respect to the mixture critical temperature of  $C_6H_{14} - N_2$   
 324 at  $P_{ch} = 5MPa$ , n-hexane is injected in subcritical state when it is at 480K and it is injected in a  
 325 supercritical state when it is heated to 560K or 600K. The three simulation cases are summarized  
 326 in Table 2, where  $T_{i,C_6H_{14}}$  is the temperature in the injector reservoir. The temperature  $T_{C_6H_{14}}$   
 327 as well as the mean velocity at the nozzle exit  $u_{C_6H_{14}}$  were calculated based on the assumption of an  
 328 isentropic nozzle flow as explained by Traxinger et al. [21].

### 329 4.2. Configuration setup

330 Figure 6(a,b) present the boundary conditions, the computational domain, as well as the mesh  
 331 structure, respectively, employed in this study. The nozzle orifice diameter ( $D_i$ ) is  $236\mu m$ , as can  
 332 be seen in this figure on the left side of the hexahedral computational domain. The length and  
 333 width of the grid are  $90D_i$  and  $40D_i$ , respectively. These dimensions proved to be large enough  
 334 to avoid edge effects on the numerical results. The base grid size was set to  $30\mu m$ . Besides, fixed  
 335 embedding has been used to refine the grid at specific locations especially near the nozzle exit,  
 336 where the grid size was specified to be  $7.5\mu m$ . This minimum value is the same refined value  
 337 used in [21]. At the jet inlet, uniform velocity and temperature profiles for  $u_{C_6H_{14}}$  and  $T_{C_6H_{14}}$   
 338 are used, as defined in Table 2. In addition, no-turbulent fluctuations are specified at the inlet

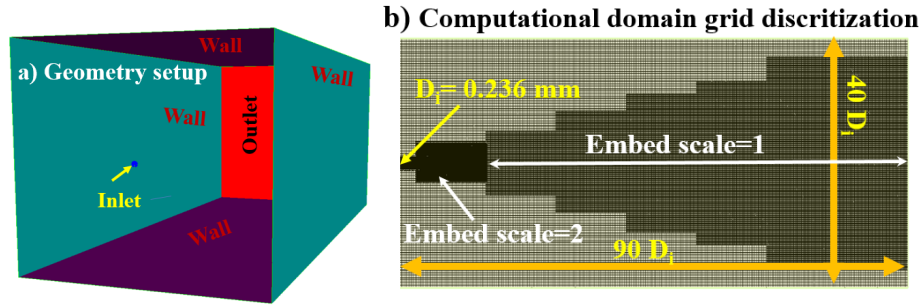


Fig. 6. Schematic of the injector setup as (a) Geometry setup, and (b) Computational domain grid discretization. Fixed embedding has been used to refine the grid at specific locations in the domain. (Local grid size = (Base grid size) /  $2^{embed\_scale}$ ). The base grid size was set to  $30\mu\text{m}$  so that the minimum grid size near the nozzle exit has been specified to be  $7.5\mu\text{m}$  using an  $embed\_scale = 2$ .

339 injection boundary. A pressure outflow boundary condition is used for the outlet boundary. The  
 340 chamber pressure for all the cases were set to  $P_{ch} = 5\text{MPa}$ . No-slip and adiabatic conditions are  
 341 specified for the walls indicated in Figure 6(a). The time step is automatically adjusted in the  
 342 solver based on a maximum Courant-Friedrichs-Lewy (CFL) number of 50 reaching a value in  
 343 the range of  $[10^{-8} - 10^{-9}]$  seconds.

344

#### 345 4.3. RFM model results

346 Figure 7(a,b), respectively, shows the numerical results of the RFM model, obtained when the  
 347 LES-Sigma turbulence model [42] is employed, in terms of mixing temperatures versus AMT for  
 348 the three different test cases (T480, T560, and T600) defined in Table 2. Specifically, Figure  
 349 7(a) demonstrates a good agreement between the predicted phase boundary calculated in this  
 350 study compared with [21]. The low scattering of the LES mixing temperatures in Figure 7(a)  
 351 indicates almost adiabatic mixing injection (between n-hexane and  $N_2$ ). The graphical insert  
 352 shows that the LES mixing temperature scatter plots for the T560 case do intersect the dew line,  
 353 enter the two-phase region and may induce condensation. Figure 7(b) includes the theoretical  
 354 AMT (defined in Section 3.5) for the three cases and show the same behavior as the RFM model  
 355 for case T560.

356 In Figure 8(a-c), the experimental single-shot images of [21] (left frame 1) are qualitatively

Table 2. Operating conditions used for the current numerical study similar to the experimental study of [21].

Case	$P_{ch}[\text{MPa}]$	$T_{ch}[\text{K}]$	$T_{t,C_6H_{14}}[\text{K}]$	$T_{C_6H_{14}}[\text{K}]$	$u_{C_6H_{14}}[\text{m/s}]$	Injection state
T480	5	293	480	479.3	51	subcritical
T560	5	293	560	554.8	72.1	supercritical (condensing)
T600	5	293	600	595	90.3	supercritical

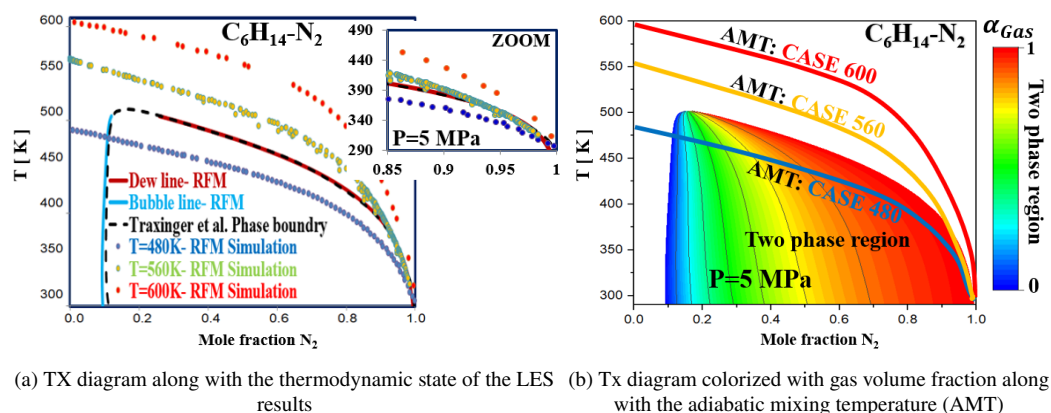
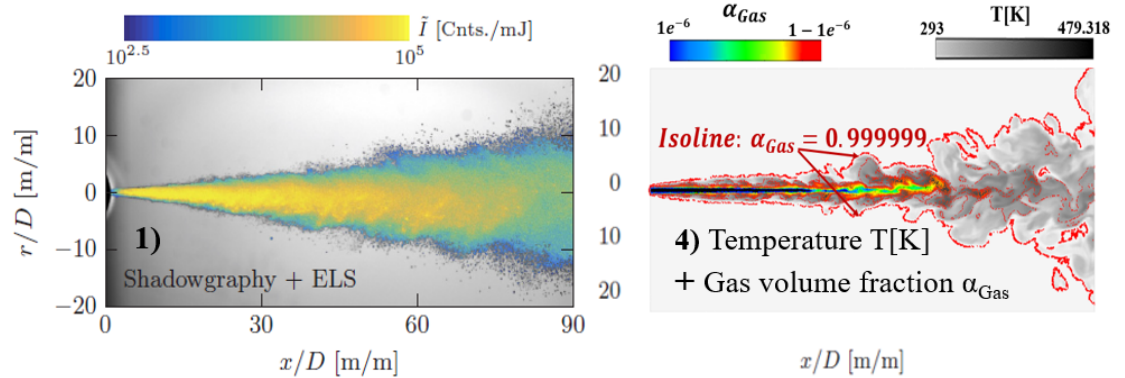


Fig. 7. Temperature  $N_2$ -composition phase diagram for binary mixture of  $C_6H_{14} - N_2$  at  $P=5$  MPa, calculated by PR-EoS along with the adiabatic mixing temperature (AMT). (a) includes the comparison with [21] along with the three scatter plots of the numerical LES mixing temperature results. The low scattering of the LES mixing temperatures indicate almost adiabatic injection flows. The graphical insert shows that the LES mixing temperature scatterplots for the T560 case do intersect the dew line and enter the two-phase region. (b) includes the theoretical AMT for the three cases and show the same behavior as the RFM model for case T560. The two-phase region background is colored by the gas volume fraction values.

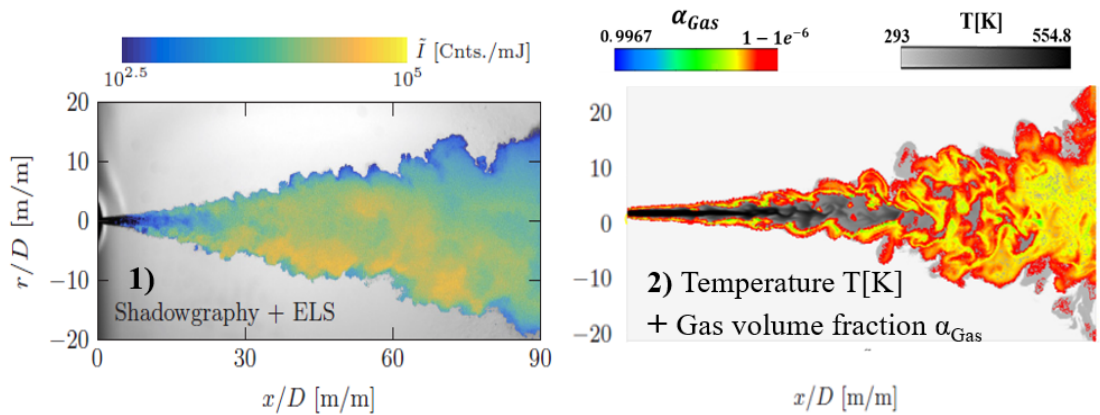
357 compared with instantaneous numerical snapshots (right frame 2) for the three cases (T480,  
 358 T560, and T600) obtained using the RFM model, when the LES-Sigma turbulence model [42]  
 359 is employed. For the experiments, the elastic light scattering (ELS) images superimposed onto  
 360 shadowgraph images, to visualize both the flow structure and the thermodynamic state. Similarly  
 361 for the numerical side, the gas volume fraction  $\alpha_{Gas}$  distribution is superimposed onto the  
 362 temperature contours in a plane passing through the axis of the nozzle to indicate regions of  
 363 two-phase flow and especially the lowest values of  $\alpha_{Gas}$  near the periphery of the jet. These  
 364 numerical results were taken at a point in time so that the jet could be considered as quasi-steady.  
 365 In doing so, a direct comparison of the two-phase droplet regions in the experiment and LES is  
 366 rendered in Figure 8(a-b).

367 More precisely, in the subcritical Case T480, n-hexane is injected in a liquid state as depicted in  
 368 blue color in Figure 7(b) indicating tiny  $\alpha_{Gas}$  in the liquid core. In this case, a classical atomizing  
 369 jet is shown experimentally in Figure 8(a). A spray can be seen clearly in this (shadowgraph  
 370 + ELS) experimental image with distinct droplets at the periphery of the jet (especially for  
 371  $X/D > 50$ ). Also, the ELS experiments have revealed a strong phase separation within the jet  
 372 by showing high scattering intensity, (see I the palettes shown in Figure 8). Turbulent diffusion  
 373 of  $N_2$  into the injected n-hexane liquid core causes this mixture to enter the two-phase dome  
 374 at a mole fraction of  $N_2$  of about 0.1, as shown in Figure 7. This strong phase change can be  
 375 seen in the numerical result shown in Figure 8(a) where the liquid core is represented (in blue)  
 376 as the low gas fraction region. The rest of jet is in two-phase state representing the droplets  
 377 spray and highlighting the flow structure at its periphery. This flow structures can be also seen in  
 378 Figure 9 which demonstrates the temporal evolution of superposed temperature and gas volume  
 379 fraction ( $\alpha_{Gas}$ ) contours. It is worth noting on Figure 9 that the two-phase jet can be considered  
 380 as quasi-steady for  $t > 4$  ms. Also, the authors would like to remind here that surface tension is not  
 381 taken into account in the proposed RFM model and that future work should verify its effect on  
 382 the numerical results of the subcritical T480 case.

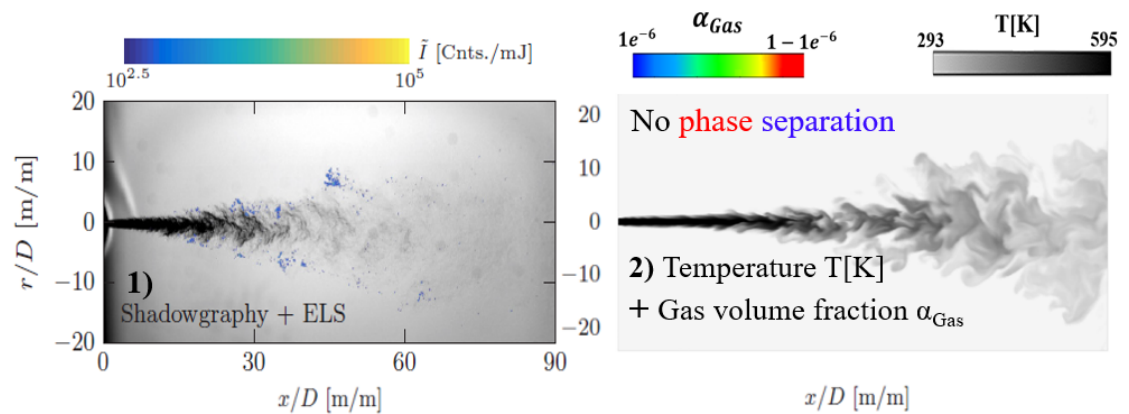
383 For the second case T560, n-hexane is injected at a supercritical liquid-like state into  $N_2$  which is



(a) Case T480



(b) Case T560



(c) Case T600

Fig. 8. Comparison of experimental (left(1)) and numerical snapshots (right(2)) for the three test cases (T480, T560, and T600). The ELS image superimposed onto the corresponding shadowgraph are used to visualize both the flow structure as well as the thermodynamic state (adapted from [21]) in quasi-steady state condition.  $\alpha_{Gas}$  is the gas volume fraction

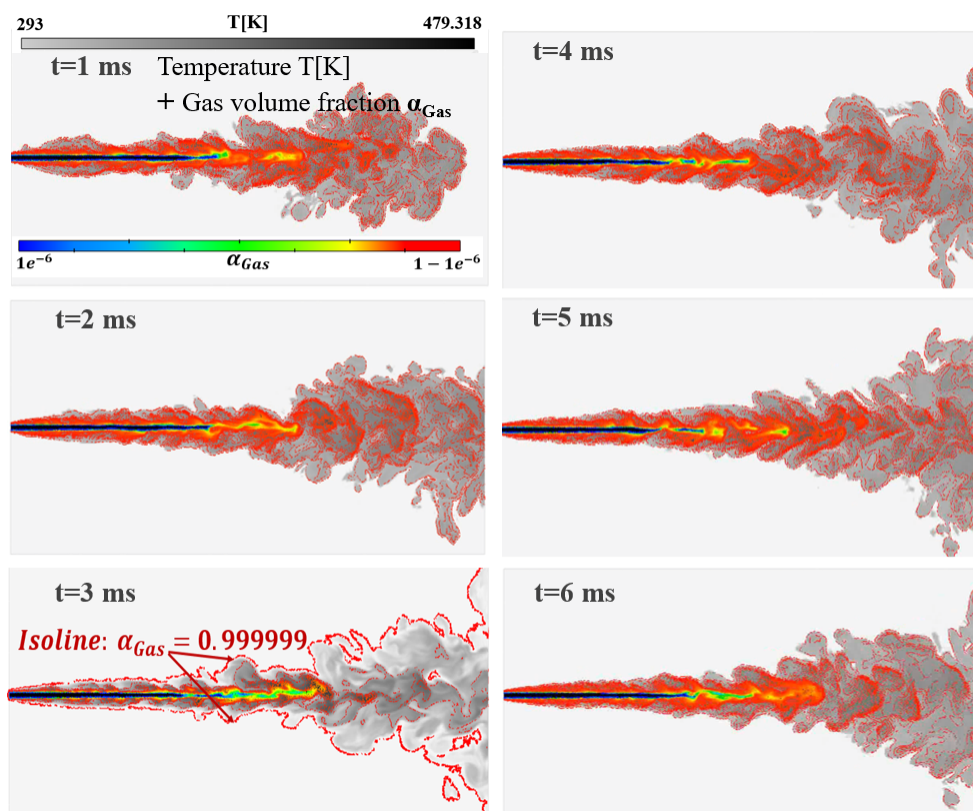


Fig. 9. Temporal evolution of (temperature +gas volume fraction( $\alpha_{Gas}$ )) contours using Sigma turbulence model for case T=480.

384 at supercritical state as well. Although this supercritical condition, the shadowgraph + ELS image  
 385 (Figure 8(b)) has revealed very rough borders indicating the presence of droplet clusters. This  
 386 interesting phase change phenomena can be further discussed here using Figure 7(a). Indeed, the  
 387 zoom inserted in this figure shows that the LES mixing temperature scatter plots for the T560 case  
 388 has crossed the two-phase dome at high  $N_2$  mole fraction. This means that most of the droplets  
 389 nucleus have appeared close to the jet periphery. This phase change can be seen in the numerical  
 390 results of Figure 8(b) and in more detailed time evolution of the jet in Figure 10, in which  
 391 very low liquid volume fraction is highlighted (see the palette where the value of gas volume  
 392 fraction changes from around 0.9967 to unity). In this case, the good qualitative validation of  
 393 the appearance of liquid by condensation at the periphery of the jet could be considered as an a  
 394 posteriori justification of the VLE assumption on which the proposed RFM model is based.

395 Finally, for case T600, Figure 7(a,b) demonstrates, the jet does not experience any phase change  
 396 and two-phase regime. Hence, with respect to the mixture critical point, the jet undergoes a single  
 397 phase mixing regime. The shadowgraph + ELS experiments have revealed this single-phase  
 398 regime within the jet by showing no significant scattering signal, as shown in Figure 8(c). As  
 399 shown in this figure, this single-phase (dense-gas) behavior within the jet has been also well  
 400 predicted by the RFM model.

401 It is worth noting that the comparison between the simulation and the experiment has shown  
 402 some differences regarding the jet penetration length and dispersion. This can be attributed  
 403 to the experimental uncertainty of the velocity and unknown turbulence at the nozzle exit. In  
 404 addition, there is some probability of uncertainty in the numerical simulation as well. However,

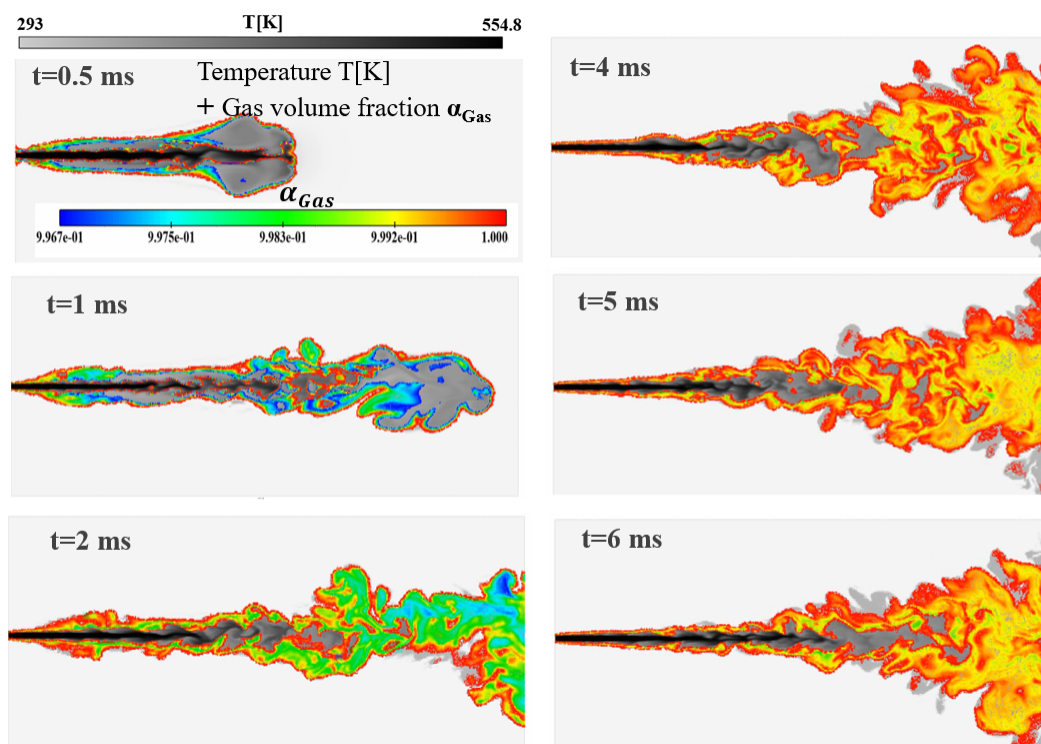


Fig. 10. Temporal evolution of (temperature +gas volume fraction ( $\alpha_{Gas}$ )) contours using Sigma turbulence model for case 560 (see table 2).

405 the current validation has demonstrated that the RFM model can efficiently capture the main  
 406 physics in various conditions.

#### 407 4.4. Analysis of droplet formation process for binary systems at supercritical regime

408 With the phase equilibrium model employed in this study, a detailed analysis of the droplet  
 409 formation process becomes possible in the condition the metastability relaxation time is smaller  
 410 than the CFD time step. Obviously, VLE assumption is not valid in case the metastability duration  
 411 is much longer than the CFD time step. In this case, detailed models for nucleation and droplet  
 412 growth under non-equilibrium condition are required [54].

413 Here, the case T560 is discussed based on Figure 11(a-d) in order to further illustrate the phase  
 414 transition and droplet formation near to the jet border of an initially supercritical n-hexane fluid  
 415 ( $T_{inj} > T_c$ ) due to the interaction with its surrounding supercritical nitrogen. More specifically,  
 416 Figure 11 shows the contour plots of a) the temperature, b) the  $C_6H_{14}$  mass fraction in the  
 417 mixture, c) the phase indicator  $\text{PHI} = 1, 2$  which designates the gas state and the two-phase state,  
 418 respectively, and finally d) the  $C_6H_{14}$  mass fraction in the liquid phase defined as follows: The  
 419 mass fraction of each component ( $k$ ) in any phase ( $p$ ), ( $Y_{k,p}$ ) is  
 420 defined as the ratio of component ( $k$ ) density in the phase ( $p$ ) considered with respect to the  
 421 phase density ( $\rho_p$ ), as  $Y_{k,p} = \frac{\alpha_p \rho_{k,p}}{\sum_k \alpha_p \rho_{k,p}}$ .

422 As the phase indicator shows in Figure 11(c), the periphery of the jet goes to two phase regions.  
 423 This can also be seen in the mass fraction contour of  $C_6H_{14}$ , in Figure 11(b). In this figure, a  
 424 small mass fraction of  $C_6H_{14}$  (black color) is present near the boundary of the jet at near room  
 425 temperature (light gray color in the temperature contour in Figure 11(a)). More importantly,

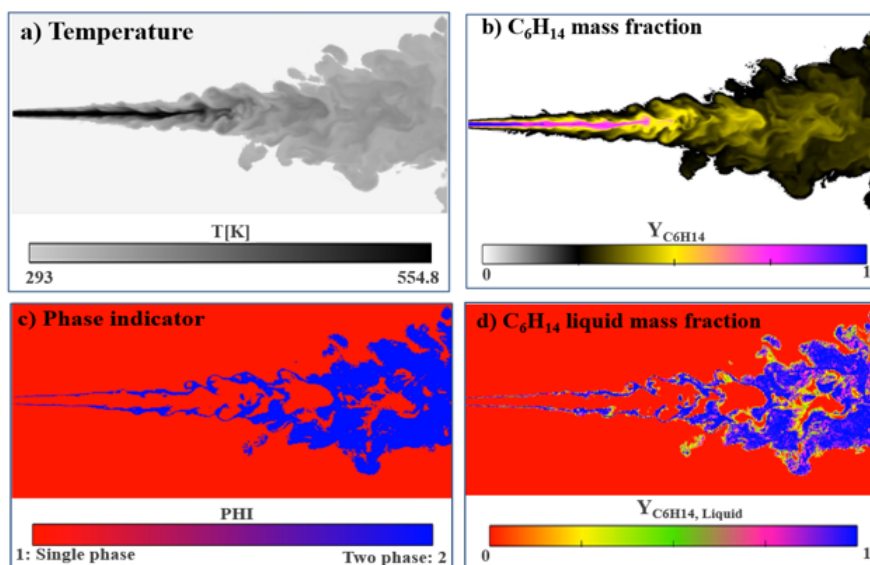


Fig. 11. T560 case results: contour plot of (a) Temperature, (b)  $C_6H_{14}$  mass fraction, (c) Phase indicator in which  $PHI=1, 2$  denotes single phase and two-phase states, respectively, and (d)  $C_6H_{14}$  liquid mass fraction. This mass fraction ( $Y_{C_6H_{14},l}$ ) is defined as the ratio of  $C_6H_{14}$  density in the liquid phase (index  $l$ ) with respect to the liquid density ( $\rho_l$ ), as  $Y_{C_6H_{14},l} = \alpha_l \rho_{C_6H_{14},l} / \rho_l$ .

426 Figure 11(d) reveals the mass fraction of  $C_6H_{14}$  in the liquid phase formed by condensation,  
 427 mostly near the jet periphery. It worth to mention that as  $\sum_k Y_{k,l} = 1$ , the mass fraction of  $N_2$  in  
 428 the liquid phase formed by condensation is revealed to be very small in Figure 11(d).

#### 429 4.5. Turbulence modelling impacts on two phase jets

430 Turbulence is known to significantly enhance the mixing rate of species, momentum and energy.  
 431 This convective process occurs at different length scales as it results from the occurrence of  
 432 turbulent eddies with different characteristic sizes, in high Reynolds number flows. Currently,  
 433 only the direct numerical simulation (DNS) method can handle turbulent flows, but only for  
 434 single-phase gas flows. In general, if a simulation does not use a sufficiently refined grid (DNS),  
 435 it cannot properly account for turbulent mixing effects. This is still not practical in most of  
 436 industrial test cases. Thus, turbulence models are often employed to estimate the additional  
 437 mixing due to turbulence. As Richard Feynman (the American theoretical physicist, Nobel Prize  
 438 in Physics in 1965) mentioned: "Turbulence is the most important unsolved problem of classical  
 439 physics", hence developing a general turbulence model is still complicated due to highly unsteady  
 440 and intricate interactions between various physical phenomena (turbulence, mixing, multi-phase  
 441 flows, etc.) along with complex geometries and diverse boundary conditions. Traditionally,  
 442 RANS (Reynolds-averaged Navier–Stokes equations) models [44] employ an effective turbulent  
 443 viscosity to model the Reynolds stress term. Besides, in the past few years, Large-Eddy Simulation  
 444 (LES) [42, 43] as a promising approach for turbulence modeling has been extensively used  
 445 due to its unique potential to reproduce these unsteady and irregular phenomena. The main  
 446 difference between LES and RANS models is how the fields are decomposed for modeling. For  
 447 RANS approaches, the field is decomposed into an ensemble mean and a fluctuating component.  
 448 However, LES resolves more of the turbulent spectrum by using a more refined grid in such  
 449 a way that only the isotropic smallest eddies remain for an easier modelling of sub-grid scale.

450 Hence, for LES approach, the field is decomposed into a resolved field and a sub-grid field,  
 451 and numerous LES models have been developed to relate the turbulent stresses to a differential  
 452 operator acting on the resolved velocity field, as Equations (10 - 12). However, recent studies  
 453 still demonstrate that each approach has some cons and pros, and choosing the best global LES  
 454 approach for turbulence modeling, especially for internal combustion engines, is a crucial issue  
 455 due to appearance of various complex phenomena [56, 57]. The oldest and most commonly  
 456 used approach is the one proposed by Smagorinsky [43]. This model, known as a zero-equation  
 457 LES model, does not solve any additional transport equations for sub-grid scale. It relates the  
 458 turbulent viscosity to the magnitude of the strain rate tensor and the filter (usually taken as the  
 459 cell size). Besides, an other promising zero-equation sub-grid model, called the Sigma model,  
 460 has been developed by Baya-Toda et al. [43]. This more recent model shows that it can be a better  
 461 alternative to the Smagorinsky model. It constructs the turbulent viscosity from the singular  
 462 values of the resolved velocity gradient tensor. Most of the performance study of Sigma model  
 463 have been performed for combustion [56, 57], and not for two-phase flows. In addition, two-phase  
 464 turbulence effects have largely been neglected in the current literature. Indeed, most of the  
 465 current state of the art two-phase flow simulations still consider one-fluid turbulence modelling  
 466 approach, i.e. assuming that the turbulent structures behave similarly to single-phase turbulence.  
 467 In this study, the objective is to give some insight to two-phase turbulence modelling by analyzing  
 468 the interaction between the turbulence and two-phase flows, especially when phase transition  
 469 (evaporation, condensation) occurs. Generally, the turbulent viscosity in LES zero-equation  
 470 models are defined as the following Equation 10.

$$\nu_{SGS} = (C_m \bar{\Delta})^2 \bar{D}_m \quad (10)$$

471 where  $C_m$  and  $D_m$  are the model ( $m$ ) specific constant, and differential operator of the model  
 472 respectively.  $\bar{\Delta}$  is the filter width (i.e. the cell size in the context of LES with implicit filtering).  
 473  $D_m$  as the differential operator of the Smagorinsky and Sigma models are computed as the  
 474 following Equations (11-12).

$$\bar{D}_{Smag} = \bar{S} = \sqrt{2\bar{S}_{ij}\bar{S}_{ij}}, \bar{S}_{ij} = 0.5\left(\frac{\partial\bar{u}_i}{\partial x_j} + \frac{\partial\bar{u}_j}{\partial x_i}\right) \quad (11)$$

475

$$\bar{D}_{Sigma} = \frac{\sigma_3(\sigma_1 - \sigma_2)(\sigma_2 - \sigma_3)}{\sigma_1^2} \quad (12)$$

476 The differential operator of the Smagorinsky model is based on the resolved characteristic  
 477 rate of strain ( $\bar{S}_{ij}$ ). However, the Sigma model employs the singular values of the resolved  
 478 velocity gradient tensor so that the singular values  $\sigma_i$  ( $\sigma_1 \geq \sigma_2 \geq \sigma_3$ ) are the square roots of the  
 479 eigenvalues of the matrix  $\bar{S}_{ij} * \bar{S}_{ji}$  [43].

480 As a final comment on the turbulence modelling, it is worth to note that turbulent viscosity ( $\mu_{SGS}$ )  
 481 is known to be much greater than laminar one ( $\mu$ ) in single-phase turbulent flows. However, this  
 482 is not always the case in turbulent two-phase flows, especially at the liquid-gas interface where  
 483 the laminar viscosity experiences a high gradient. Another important point is that the rate of  
 484 strain  $\bar{S}_{ij}$  in  $\bar{D}_m$  equations may vary significantly in the interface region due to a large phase  
 485 transition. This is also may be the case due to non-linear property ( $C_p, D_T, \dots$ ) behaviors at  
 486 supercritical state in the Widom line region. The latter two effects are somewhat included in the  
 487 proposed RFM model through the tabulation of the VLE properties and the impulse effect of the  
 488 phase change on the momentum. However, a more thorough fundamental study of the interaction  
 489 between turbulence and EoS should be conducted in future work [58].

490 Figure 12 shows instantaneous contour plot of temperature, and density for case T480 at  $t=2.5$  ms  
 491 using various turbulent models denoted as RANS, LES-Smagorinsky, and LES-Sigma models,  
 492 respectively. Noteworthy, it does not make sens to compare ensemble averaged RANS results and

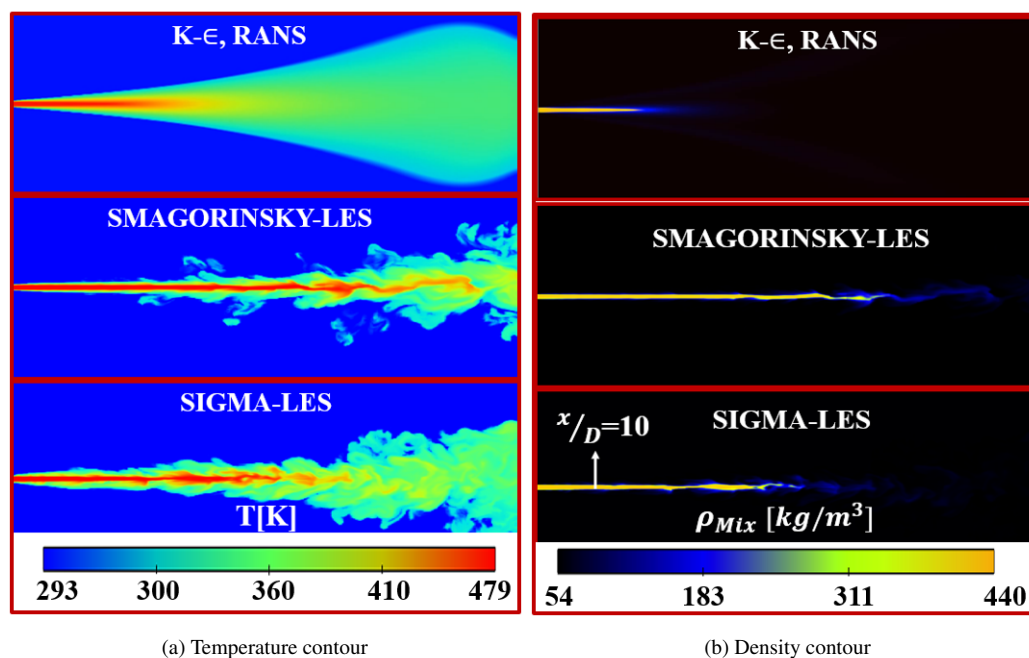


Fig. 12. Impacts of turbulence modellings of the jet structure for various properties for two phase flows using  $(k - \epsilon)$  RANS, LES-Smagorinsky, and LES-Sigma models, respectively, from top to down, at  $t=2.5$  ms.

493 instantaneous LES results. However, this Figure demonstrates the different behaviour between  
 494 RANS and LES models. The liquid core (represented by the mixture density) is very short  
 495 relatively to the LES results. This is due to the higher turbulent viscosity and kinetic energy  
 496 (TKE) generated in the RANS simulation (see also Figure 13(a,c)).  
 497 The Sigma-LES model gives an initial spray cone angle that better matches the experimental  
 498 image shown in Figure 8(a) than the LES-Smagorinsky model. Also, the liquid core obtained  
 499 with Sigma-LES model is shorter than the one obtained by LES-Smagorinsky model. This  
 500 demonstrates a higher evaporation rate obtained using the LES-Sigma model, and thus the  
 501 significant effect of turbulence modeling on such two-phase numerical results. However, more  
 502 simulations should be performed in future work to assert the superiority of LES-Sigma in  
 503 two-phase flows. To have a better insight, Figure 13(a-c) display a qualitative comparison of  
 504 some turbulent properties profiles at  $X/D = 10$  (see the arrow in Figure 12(b)), as a) Turbulent  
 505 viscosity ( $\mu_T$ ), b) Turbulent conductivity ( $\lambda_T$ ), and c) Turbulent kinetic energy (TKE) using  
 506 the different turbulence models, respectively at  $t=2.5$  ms. Figure 13(a,b) demonstrates the  
 507 huge values obtained with the RANS model relatively to the LES models. In addition, lower  
 508 turbulent viscosity and conductivity levels are obtained using the Sigma model compared to the  
 509 Smagorinsky model in the liquid-gas interface region. This lower turbulent viscosity is expected  
 510 since Sigma model has been developed to avoid overestimating the SGS turbulence in shear layers,  
 511 as also reported by [56]. Hence, this lower turbulent viscosity level has led to less dissipation of  
 512 the turbulent energy, TKE, as shown in Figure 13(c). Besides, some interesting points can be  
 513 observed in Figure 14 in which is plotted dimensionless radial profiles of the density, density  
 514 gradient, gas volume fraction and the turbulent conductivity, at  $X/D = 10$ .  
 515 First, it is important to note in this figure that the extrema of the turbulent conductivity and  
 516 density gradient almost coincide with the locus of the liquid-gas interface at  $\alpha_{Gas} = 0.5$ . This

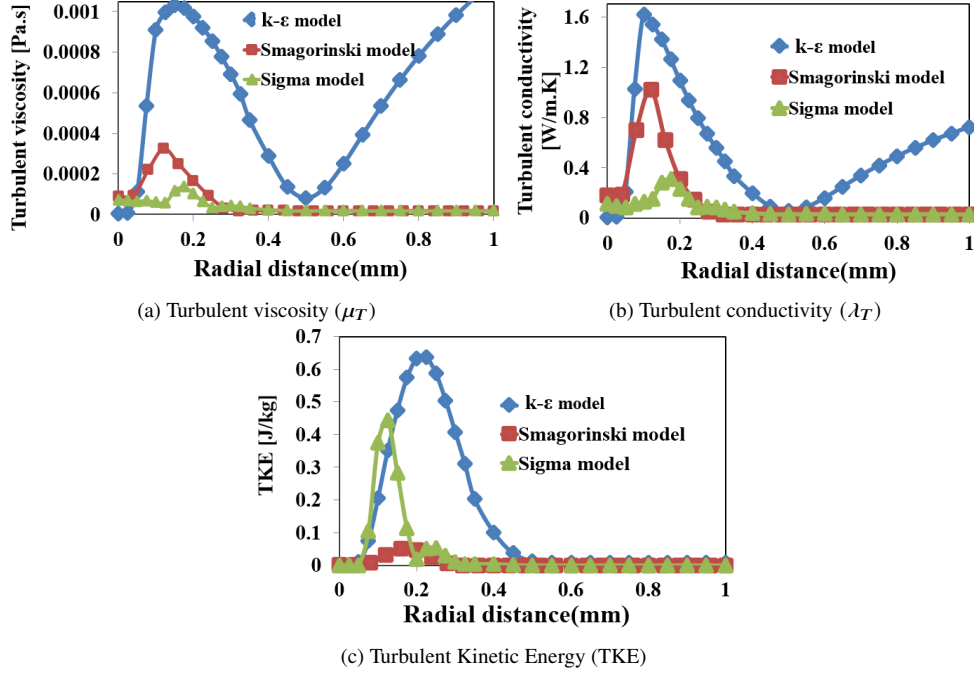


Fig. 13. Impacts of turbulence modellings on different turbulent properties using different ( $k - \epsilon$ ) RANS, LES-Smagorinsky, and LES-Sigma models, respectively, from top to down, at  $t=2.5$  ms at  $X/D = 10$ . Due to the much higher values from the ( $k - \epsilon$ ) model for the different turbulent properties, they have been divided by 100, 100, and 20 for turbulent viscosity, TKE, and turbulent conductivity, respectively, to be in the same range as LES data.

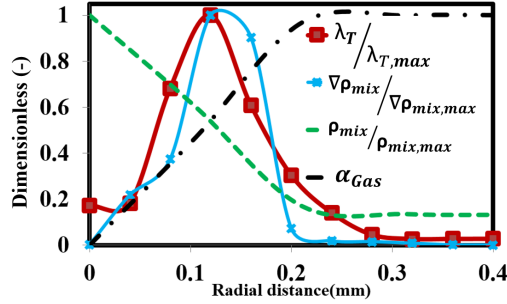


Fig. 14. Impacts of density gradient on the turbulent properties, at  $t=2.5$  ms at  $X/D = 10$ , using LES-Sigma model.

517 demonstrates the high coupling of turbulence with flow characteristics such as density gradient.  
 518 Indeed, it is well known that the density gradient in a two-phase flow plays a key role in turbulent  
 519 two-phase flows and particularly on liquid atomization.  
 520 Generally, vorticity analysis can be used as an appropriate tool for the flow mixing analysis [59,60].  
 521 the following Equation 13 gives the total derivative of vorticity  $\omega$  for compressible flows [59].

$$\frac{D\omega}{Dt} = -\omega(\nabla \cdot u) + (\omega \cdot \nabla)u + \frac{\nabla \rho * \nabla P}{\rho^2} - \nu \nabla^2 \omega \quad (13)$$

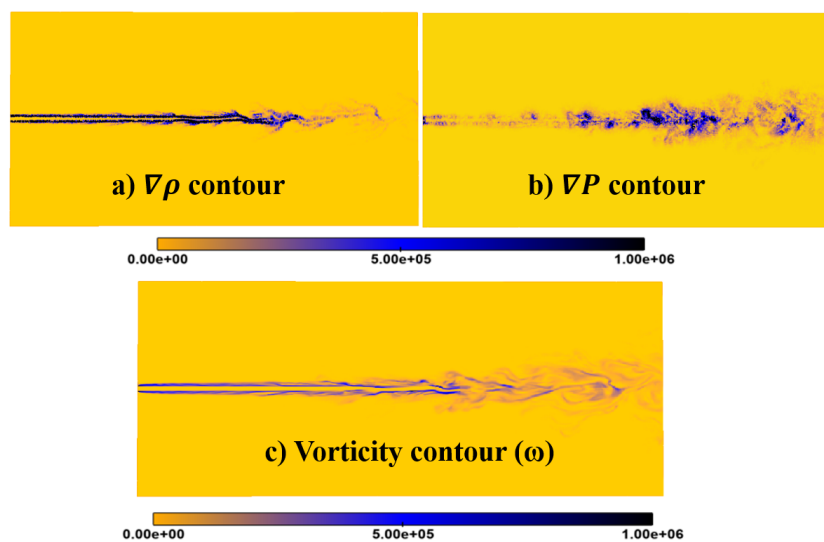


Fig. 15. (a) Density gradient, (b) Pressure gradient and (c) Vorticity contours at the interface at  $t=2.5$  ms. The misalignment of spatial pressure and density gradients is at the origin of the baroclinic torque source term.

522 The first term on the right hand side of Equation 13 represents the expansion of the vorticity due to the compressibility. The second term, called vortex stretching term, is due to the enhancement  
 523 of vorticity by stretching. The third term, called baroclinic torque, is due to the misalignment  
 524 of spatial pressure and density gradients. Finally, the viscous diffusion last term expresses the  
 525 vorticity change due to viscous dissipation. Figure 15(a,b) shows the appearance of a peak at  
 526 density and pressure gradients contours at the interface, which leads to the formation of high  
 527 vorticity in at the interface, as shown in Figure 15(c). This demonstrates that real fluid models  
 528 are required to accurately compute density and pressure gradients and to simulate such turbulent  
 529 injection flows, as recently reported by [61].  
 530

## 531 5. Quantitative validation

532 To quantitatively validate the tabulated RFM-LES results, the numerical results will be compared  
 533 in this section with the recent experimental data from Baab et al. [62]. They performed quantitative  
 534 sound speed measurements in jet mixing zones for different configurations with various mixtures  
 535 at different conditions. The n-hexane case, which corresponds to "Case 1" in Baab et al. [62] is  
 536 chosen for the comparison to our numerical results. The applied numerical setup is identical to  
 537 the one used in the previous section. The experimental conditions, listed in Table 3, are very  
 538 similar to the T600 case in Section 4, as shown in Table 2. One point is worth mentioning is  
 539 that the nozzle exit temperature  $T_e = 627K$  and velocity  $u_e = 90m/s$  were estimated in that  
 540 experimental study based on the assumption of an isentropic flow inside the injector [62].

541 In this study, another strategy has been adopted, where inflow turbulence fluctuations have been  
 542 generated and superimposed on the inflow velocity profile using Fourier method, based on the  
 543 proposals by [63]. This method has been used in order to generate correlated turbulent fluctuations  
 544 over the mean inlet profile at the nozzle exit. Using synthetic turbulence at the computational  
 545 domain inlet has shown significant effect on the spray development as demonstrated in [64, 65],  
 546 when the in nozzle flow is not included in the simulation. As pointed out in [64, 65], this  
 547 turbulent intensity ranges between 3% and 5% depending on the turbulence model. Hence, the

Table 3. Operating conditions used for the current numerical study taken from Baab et al [62] experimental study. The nozzle exit temperature  $T_e$  was estimated based on the assumption of an isentropic flow inside the injector calculated by [62].

Injection fuel	Chamber gas	$P_{ch}$ [MPa]	$T_{ch}$ [K]	$T_{t,C_6H_{14}}$ [K]	$T_{e,C_6H_{14}}$ [K]
$C_6H_{14}$	$N_2$	5	296	630	627

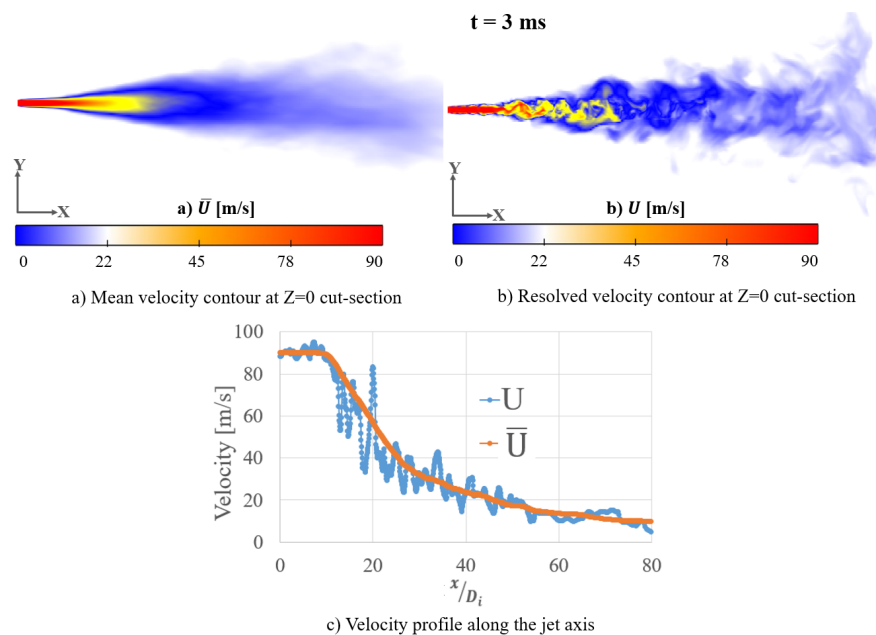


Fig. 16. (a) Mean velocity field ( $\bar{U}$ ), (b) The resolved velocity ( $U$ ) at 3 ms, and (c) The velocity profile plotted along the jet axis where the resolved velocity is at 3 ms and the mean velocity is computed using the LES results in the time interval between 2 and 3 ms after the start of injection. For this case, a fluctuating boundary condition has been superimposed on the inflow velocity profile using Fourier method with 5% intensity.

548 injection boundary conditions in this study are based on the mean inlet velocity of 90 m/s and 5%  
 549 turbulent intensity superimposed on the inflow velocity profile. In addition, n-hexane is injected  
 550 with the estimated nozzle temperature of 627K to the chamber filled by  $N_2$  at  $T_{ch} = 296K$  and  
 551  $P_{ch} = 5MPa$ . With regard to the numerical setup, the same configuration as shown in Figure 6 is  
 552 used with the base grid size set to ( $40\mu m$ ) at the far-field of nozzle, and along with different levels  
 553 of embedding to achieve a fine mesh resolution near the nozzle exit of ( $10\mu m$ ), corresponding to  
 554 26 cells in the nozzle diameter. Moreover, the time step is automatically controlled based on a  
 555 maximum CFL number of 50 reaching a value in the range (10 ns-50ns).

556 Besides, the LES-Sigma model has been used for the turbulence modeling of this test case due  
 557 to its performance, as shown in the previous section. Figure 16 demonstrates (a) The mean  
 558 velocity contours computed using the LES results in the time interval between 2 and 3 ms after  
 559 the start of injection, (b) The resolved velocity, in addition to (c) The velocity profile along the jet  
 560 axis obtained with an inlet fluctuating boundary condition with 5% intensity. Unfortunately, no  
 561 experimental velocity and turbulence data are available in this case. Therefore, these numerical  
 562 results can be used as a reference for future work.

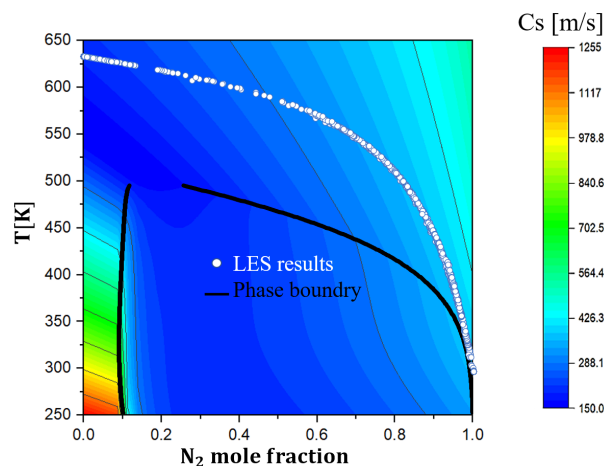


Fig. 17. Temperature- $N_2$  mole fraction diagram for binary mixture of  $N_2 - C_6H_{14}$ , colored with the mixture sound speed, using Wood formula for two phase region [66] at  $P = 5 \text{ MPa}$ , using PR-EoS, along with the phase boundary (in black). The scatter plots (white points) show the locus of the mixing temperature obtained by the RFM-LES model for the case with  $T_e = 627 \text{ K}$  simulation.

563 Figure 17 shows the Temperature- $N_2$  mole fraction diagram for the binary mixture of  $N_2 - C_6H_{14}$ ,  
 564 colored and mapped with the mixture sound speed, computed using the Wood formula [66]  
 565 for the two-phase region at  $P = 5 \text{ MPa}$ , calculated by PR-EoS, along with the scatterplots  
 566 (white points) locus of the mixing temperature obtained by the RFM-LES model. In this figure,  
 567 we can observe the sound speed variations along the mixing temperature (white dots). This  
 568 demonstrates that the flow in the current supercritical condition experiences relatively small  
 569 sound speed variations. This could be seen more precisely in Figure 18(c) which depicts the  
 570 instantaneous fully developed  $N_2 - C_6H_{14}$  LES results in terms of sound speed contour after  $t=3$   
 571 ms. Indeed, Figure 18 presents the instantaneous mixture sound speed at axial center-line and  
 572 at radial direction at  $x/D_i = 35$ , extracted from the RFM-LES results. An intensely turbulent  
 573 mixing process of n-hexane with the supercritical nitrogen ambient can be observed in Figure  
 574 18(a,b) in terms of the mixture temperature and the hexane mass fraction. The supercritical fuel  
 575 jet with higher density ( $\rho \approx 115 \text{ kg/m}^3$ ) and temperature ( $T = 627 \text{ K}$ ) enters to the chamber filled  
 576 with  $N_2$  with lower density ( $\rho \approx 58 \text{ kg/m}^3$ ) and temperature ( $T = 296 \text{ K}$ ), and then n-hexane jet  
 577 gradually mixes with  $N_2$  inside the chamber. Moreover, as Figure 18(c) shows, the sound speed  
 578 varies from  $C_{s,C_6H_{14}}(P_{ch}, T_e) = 197 \text{ m/s}$  at the exit of nozzle and  $C_{s,N_2}(P_{ch}, T_{ch}) = 360 \text{ m/s}$ .

579  
 580 Finally, quantitative comparisons of the mixture sound speed with the experimental data from  
 581 Baab et al. [62] are shown in Figure 19 along the axial and radial axis shown in 18(c). Ten  
 582 numerical profiles shown as thin gray lines denotes the RFM-LES results in the time range of  
 583  $t=2-3$  ms. Furthermore, Figure 20(a) shows the instantaneous contours of the n-hexane mole  
 584 fraction at  $Z=0$  cut section at  $t = 3 \text{ ms}$ . Besides, Figure 20 demonstrates the instantaneous  
 585 contours of the n-hexane mole fraction and the validations of LES n-hexane mole fraction with  
 586 the analytical self-similar solutions calculated by Gerber et al. [6] using REFPROP. Specifically,  
 587 some instantaneous LES results on the jet axis, as shown in Figure 20(a), are shown (colored  
 588 with gray thin lines) in the range of  $t=2-3$  ms. Also, LES simulation results at  $t=3$  ms are  
 589 highlighted. Overall, a good agreement are found in the sound speed as well as hexane mole  
 590 fraction predicted results, compared to the reference data, which demonstrate that the RFM-LES  
 591 solver is able to predict the mixing process of  $C_6H_{14}$  and  $N_2$  accurately.

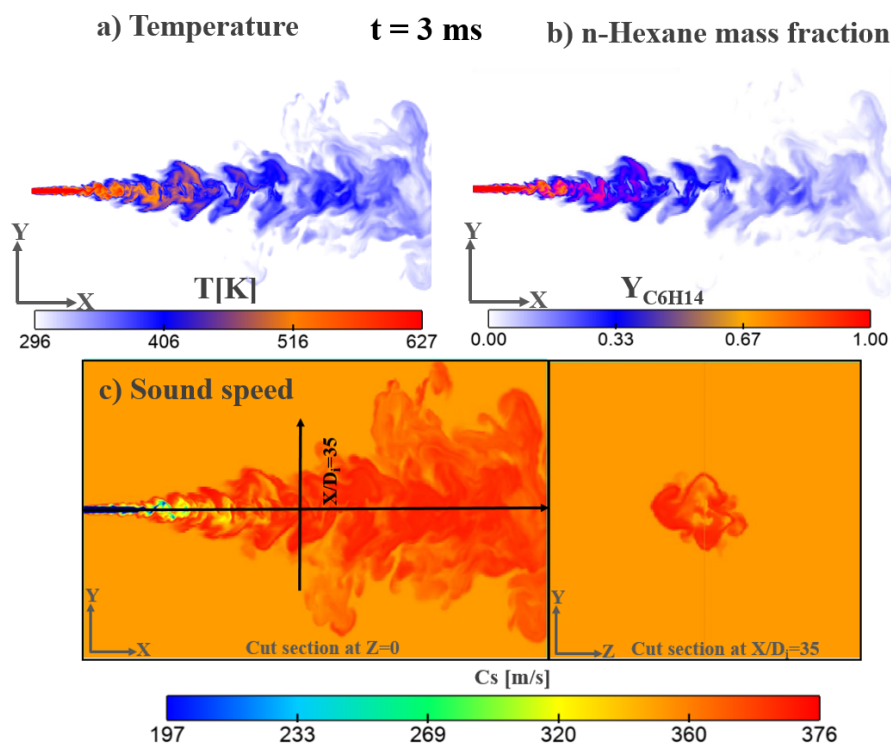


Fig. 18. The top LES results at  $t = 3 \text{ ms}$  are: (a) Instantaneous contours of the mixture temperature, (b) n-hexane mass fraction at  $Z=0$  cut section. The bottom LES results (c) at  $t = 3 \text{ ms}$  are the mixture sound speed at  $z = 0$  (left), and at  $x/D_i = 35$  cut sections (right). The sound speed in the chamber, filled initially with the  $N_2$  at  $T_{ch} = 296 \text{ K}$ , is  $C_{s,ch} \approx 360 \text{ m/s}$  (orange color). At the nozzle exit where  $T_e = 627 \text{ K}$ , the sound speed is  $C_{s,exit} \approx 197 \text{ m/s}$  (blue color).

## 592 6. Conclusion

593 In this paper, a fully compressible tabulated multicomponent real-fluid (RFM) model has been  
 594 developed in order to explore the interaction between phase separation and turbulent fluid  
 595 dynamics in multi-species supercritical flow jets. More specifically, the converge CFD solver has  
 596 been coupled to the IFPEN-Carnot thermodynamic library using a generalized tabulation method  
 597 to gain computational efficiency and robustness. This modeling approach has been implemented  
 598 in the CONVERGE solver for the simulation of the turbulent mixing of n-hexane injected in  
 599 a chamber filled with nitrogen, considering phase separation processes (condensation) at high  
 600 pressures conditions with the fluids initially at supercritical state.

601 First, n-hexane has been injected at three inflow temperatures in the same conditions as the  
 602 experimental and numerical study of Traxinger et al. [21]. Besides, a more quantitative study  
 603 has been performed using the experimental study of Baab et al. [62], which has the same setup  
 604 configuration as [17]. The obtained numerical results have been shown and proved to be in  
 605 good agreement with the experiments [21, 62]. In addition, the RFM model was shown to be  
 606 capable of simulating subcritical, transcritical and supercritical jets exhibiting phase separation  
 607 and condensation processes. As a consequence, if the jet is at a subcritical state, with regard to  
 608 the mixture critical point, it experiences the classical droplets formation process governed by the  
 609 liquid atomization. In contrast, if n-hexane is injected at supercritical state in a colder nitrogen

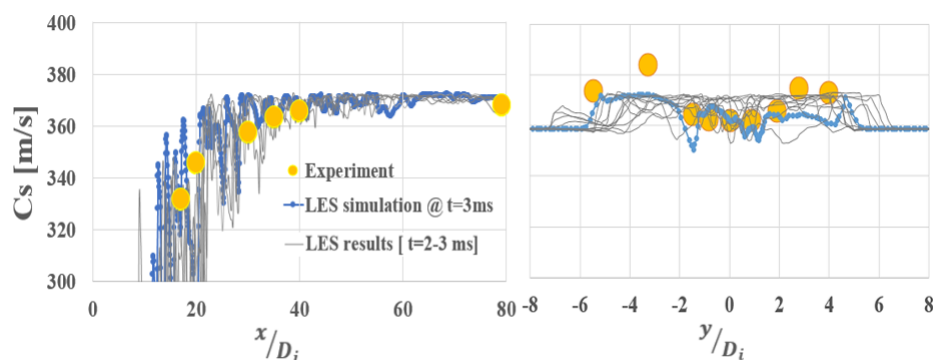


Fig. 19. Validations of mixture sound speed with experimental data of Baab et al. [62], (a) Along the jet axis, and (b) At radial direction at  $x/D_i = 35$  determined and plotted at Figure 18. LES results colored with gray thin line denotes the LES-sigma results for some instantaneous times in the range of  $t=2-3$  ms. LES simulation @  $t=3$  ms shows the variations of the mixture sound speed at  $t=3$  ms, as shown in Figure 18.

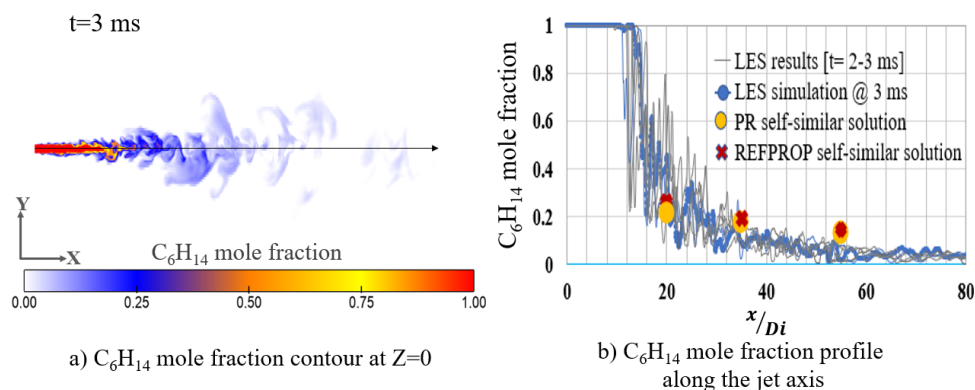


Fig. 20. Instantaneous contours of (a) n-hexane mole fraction, at  $Z=0$  cut-section at  $t = 3ms$ , and (b) Validations of LES n-hexane mole fraction, along the jet axis, with the analytical self-similar solutions calculated by Gerber et al. [6]. They hired PR EoS, and REFPROP data to analytically calculate fuel mole fraction at different distances from the nozzle exit. LES results colored with gray thin line denotes the LES-sigma results for some instantaneous times in the range of  $t=2-3$  ms. LES simulation @  $t=3$  ms, with blue color shows the variations of the n-hexane mole fraction, shown in contour plot in (a).

610 ambient, it may cross the two-phase dome, thus leading to local condensation and droplets  
 611 formation mainly at the periphery of the jet. It has been also shown that such condensation does  
 612 not occur if the n-hexane is injected at a sufficiently high supercritical temperature.  
 613 Next, comparisons between different turbulence models, including large eddy simulation models  
 614 (LES Sigma and Smagorinsky) and a Reynolds-averaged Navier-Stokes model (RANS  $K - \epsilon$ ),  
 615 have demonstrated the importance of a proper turbulence modeling, and the suitability of the  
 616 LES-Sigma model, in addition to accurate thermodynamic and transport properties, for these  
 617 highly complex jet flows. Finally, compared to our previous studies [17, 25], the computational  
 618 efficiency, accuracy, and robustness of this proposed tabulated RFM model as a remedy to the  
 619 direct evaluation of costly phase equilibrium solver have been confirmed.

## 620 7. Acknowledgements

621 This project has received funding from the European Union Horizon 2020 Research and Innovation  
 622 programme. Grant Agreement no. 861002 for the EDEM project. The authors would like to  
 623 acknowledge Dr. Angela Di Lella for her supports, and for providing the thermodynamic library,  
 624 IFPEN-CARNOT. The authors also would like to thanks Dr. Christoph Traxinger from the  
 625 Institute for Thermodynamics, Bundeswehr University Munich, Germany, for the explanations  
 626 about the sound speed measurements.

## 627 References

- 628 1. C. Crua, J. Manin, L.M. Pickett, On the transcritical mixing of fuels at diesel engine conditions, *Fuel* (2017), pp.  
 629 535-548, <https://doi.org/10.1016/j.fuel.2017.06.091>.
- 630 2. L. Jofre, J. Urzay, Transcritical diffuse-interface hydrodynamics of propellants in high-pressure combus-  
 631 tors of chemical propulsion systems, *Progress in Energy and Combustion Science* (2021), Volume 82,  
 632 <https://doi.org/10.1016/j.peccs.2020.100877>.
- 633 3. D.T Banuti, Crossing the Widom-line—Supercritical pseudo-boiling. *J. Supercrit. Fluids* (2015), 98, 12–16,  
 634 <https://doi.org/10.1016/j.supflu.2014.12.019>.
- 635 4. P.E. Lapenna, Characterization of pseudo-boiling in a transcritical nitrogen jet, *Phys. Fluids* (2018), 30 (7), p. 077106,  
 636 <https://doi.org/10.1063/1.5038674>.
- 637 5. T. Schmitt, L. Selle, B. Cuenot, and T. Poinot, Large-eddy simulation of transcritical flows, *Comptes Rendus*  
 638 *Mécanique* (2009), 337, <https://doi.org/10.1016/j.crme.2009.06.022>.
- 639 6. V. Gerber, S. Baab, F. J. Förster, H. Mandler, B. Weigand, and G. Lamanna, Fluid injection with su-  
 640 percritical reservoir conditions: overview on morphology and mixing, *J. Supercrit. Fluids* (2020), 105097,  
 641 <http://dx.doi.org/10.1016/j.supflu.2020.105097>.
- 642 7. V. Gerber, S. Baab, B. Weigand, G. Lamanna, Enhanced Rayleigh scattering in supercritical fluid injection across the  
 643 Widom line, *Atomization and Sprays*, Vol. 30, No. 12 (2020), pp. 881–893.
- 644 8. S. Jafari, H. Gaballa, CH. Habchi, and J.C De Hemptinne, Towards understanding the structure of subcriti-  
 645 cal and transcritical liquid-gas interfaces using a tabulated real fluid modeling approach, *J. Energies* (2021),  
 646 <https://doi.org/10.3390/en14185621>.
- 647 9. P.C. Ma, H. Wu, D.T Banuti, M. Ihme, On the numerical behavior of diffuse-interface methods for transcritical real-  
 648 fluids simulations, *Int. J. Multiph. Flow* (2019) 113, 231–249, <https://doi.org/10.1016/j.ijmultiphaseflow.2019.01.015>.
- 649 10. G.G. Simeoni, T. Bryk, F.A. Gorelli, M. Krisch, G. Ruocco, M. Santoro, T.Scopigno, The Widom line as the crossover  
 650 between liquid-like and gas-like behaviour in supercritical fluids, *Nat. Phys.* 6 (7) (2010) 503–507.
- 651 11. F. Gorelli, M. Santoro, T. Scopigno, M. Krisch, G. Ruocco, Liquid like behavior of supercritical fluids, *Phys. Rev.*  
 652 *Lett.* 97 (24) (2006).
- 653 12. F. A. Gorelli, T. Bryk, M. Krisch, G. Ruocco, M. Santoro, T. Scopigno, Dynamics and Thermodynamics beyond the  
 654 critical point, *Scientific Report* Vol. 3 (2013) 1203 DOI: 10.1038/srep01203
- 655 13. T. Andrews, XVIII. The Bakerian lecture—On the continuity of the gaseous and liquid states of matter, *Philos. Trans.*  
 656 *R. Soc. London* 1869, 159, 575, <https://doi.org/10.1098/rstl.1869.0021>.
- 657 14. J-P Delplanque and W. A. Sirignano, Transcritical Vaporization of Liquid Fuels and Propellants, *J. of Propulsion and*  
 658 *Power* (1999), Vol. 15, No. 6, November-December, pp. 896-902, <https://doi.org/10.2514/2.5513>.
- 659 15. B. Chehroudi, D. Talley, W. Mayer, R. Branam, J.J. Smith, A. Schik, M. Oswald, Understanding injection into high  
 660 pressure supercritical environments. Fifth international symposium on liquid space propulsion, long life combustion  
 661 devices technology, NASA Marshall Spaceflight Center, Huntsville (2003), pp. 27-30.
- 662 16. J. Bellan, Supercritical (and subcritical) fluid behavior and modeling: Drops, streams, shear and mixing layers, jets  
 663 and sprays, *Progress in Energy and Combustion Science* (2000), 26 (4-6):329–366, [https://doi.org/10.1016/S0360-1285\(00\)00008-3](https://doi.org/10.1016/S0360-1285(00)00008-3).
- 664 17. P. Yi, S. Yang, C. Habchi, R. Lugo, A multicomponent real-fluid fully compressible four-equation model for two-phase  
 665 flow with phase change, *Phys. Fluids* 31 (2) (2019), 026102, <https://doi.org/10.1063/1.5065781>.
- 666 18. A. Romei, G. Persico, Computational fluid-dynamic modelling of two-phase compressible flows of carbon diox-  
 667 ide in supercritical conditions (2021), *Applied Thermal Engineering*, Volume 190, 116816, ISSN 1359-4311,  
 668 <https://doi.org/10.1016/j.applthermaleng.2021.116816>.
- 669 19. W.O. Mayer, A. Schik, M. Schaffler, H. Tamura, Injection and mixing processes in high-pressure liquid oxygen/gaseous  
 670 hydrogen rocket combustors. *J Propul and Power* (2000), pp. 823-828, <https://doi.org/10.2514/2.5647>.
- 671 20. A. Roy, C. Joly, and C. Segal, Disintegrating supercritical jets in a subcritical environment, *J. FluidMech* (2013), 717,  
 672 193, <https://doi.org/10.1017/jfm.2012.566>.
- 673 21. C. Traxinger, M. Pfitzner, S. Baab, and G. Lamana, Experimental and numerical investigation of phase separa-  
 674 tion due to multicomponent mixing at high-pressure conditions, *Phys. Rev. Fluids* (2019), vol. 4, p. 074303,  
 675 <https://doi.org/10.1103/PhysRevFluids.4.074303>.
- 676 22. L. Qiu, and R. D. Reitz, Simulation of supercritical fuel injection with condensation, *Int J Heat Mass Transf* (2014),  
 677 pp. 1070-1086, <https://doi.org/10.1016/j.ijheatmasstransfer.2014.08.081>.

- 679 23. P. Tudisco, and S. Menon, Numerical investigations of phase-separation during multicomponent mixing at super-critical  
680 conditions, *Flow Turbulence Combust* (2019), pp. 693–724, <https://doi.org/10.1007/s10494-019-00101-4>.
- 681 24. J. Matheis, and S. Hickel, multicomponent vapor-liquid equilibrium model for LES of high-pressure  
682 fuel injection and application to ecn spray a, *Int. J. Multiphas. Flow* (2018), vol. 99, pp. 294–311,  
683 <https://doi.org/10.1016/j.ijmultiphaseflow.2017.11.001>.
- 684 25. S. Yang, P. Yi, and C. Habchi, Real-fluid injection modeling and LES simulation of the ECN Spray A in-  
685 jector using a fully compressible two-phase flow approach. *Int. J. Multiphas. Flow* (2020), 122: p. 103145,  
686 <https://doi.org/10.1016/j.ijmultiphaseflow.2019.103145>.
- 687 26. K. Nishikawa, A.A. Arai, T. Morita, Density fluctuation of supercritical fluids obtained from small-angle X-ray  
688 scattering experiment and thermodynamic calculation, *J. Supercrit. Fluids*, vol. 30, no. 3, pp. 249–257, 2004.
- 689 27. M.L. Michelsen, The isothermal flash problem. Part I. Stability, *Fluid Phase Equilibria*, Volume 9, Issue 1, 1982,  
690 Pages 1-19, [https://doi.org/10.1016/0378-3812\(82\)85001-2](https://doi.org/10.1016/0378-3812(82)85001-2).
- 691 28. M.L. Michelsen, The isothermal flash problem. Part II. Phase-split calculation, *Fluid Phase Equilibria* (1982), Volume  
692 9, Issue 1, Pages 21-40, ISSN 0378-3812, [https://doi.org/10.1016/0378-3812\(82\)85002-4](https://doi.org/10.1016/0378-3812(82)85002-4).
- 693 29. S. Saha, and J. J. Carroll, The isoenergetic-isochoric flash, *Fluid Phase Equilib.* (1997), vol. 138, pp. 23–41,  
694 [https://doi.org/10.1016/S0378-3812\(97\)00151-9](https://doi.org/10.1016/S0378-3812(97)00151-9).
- 695 30. P. Koukouvinis, A. Vidal-Roncero, C. Rodriguez, M. Gavaises; and L. Pickett, High pressure/high tempera-  
696 ture multiphase simulations of dodecane injection to nitrogen: application on ECN Spray a, *Fuel* (2020), 275,  
697 <https://doi.org/10.1016/j.fuel.2020.117871>.
- 698 31. M.De Lorenzo, P. Lafon, M.Di Matteo, M. Pelanti, J.M. Seynhaeve, and Y. Bartosiewicz, Homogeneous two-phase  
699 flow models and accurate steam-water table look-up method for fast transient simulations, *Int. J. Multiphas. Flow*  
700 (2017), 95 :199219, <https://doi.org/10.1016/j.ijmultiphaseflow.2017.06.001>.
- 701 32. S. Brown, L. Peristeras, S. Martynov, R.T.J. Porter, H. Mahgerefteh, I. Nikolaidis, G. Boulougouris, D. Tsangaris, and  
702 I. Economou, Thermodynamic interpolation for the simulation of two-phase flow of non-ideal mixtures, *Computers*  
703 *Chemical Engineering* (2016), 95, pp. 49-57, <https://doi.org/10.1016/j.compchemeng.2016.09.005>.
- 704 33. AR. Azimian, J. Arriagada, and M. Assadi, Generation of steam tables using artificial neural networks, *Heat Transfer*  
705 *Engineering* (2010), vol. 25, no. 2, pp. 41-51, <https://doi.org/10.1080/01457630490276132>.
- 706 34. Y. Fang, M. De Lorenzo, Ph. Lafon, S. Poncet, and Y. Bartosiewicz, An Accurate and Efficient Look-up Table  
707 Equation of State for Two-phase Compressible Flow Simulations of Carbon Dioxide. *Ind. Eng. Chem. Res.* (2018),  
708 57, 22, 7676–7691, <https://doi.org/10.1021/acs.iecr.8b00507>
- 709 35. F. Foll, T. Hitz, C. Muller, C.D. Munz, and M. Dumbser, On the use of tabulated equations of state for multi-phase  
710 simulations in the homogeneous equilibrium limit, *Shock Waves* (2019), 29 769–793. [https://doi.org/10.1007/s00193-](https://doi.org/10.1007/s00193-019-00896-1)  
711 019-00896-1.
- 712 36. S. Praneeth, and J.-P. Hickey, Uncertainty quantification of tabulated supercritical thermodynamics for compressible  
713 Navier–Stokes solvers, *Computational Physics* (2018), <https://arxiv.org/abs/1801.06562v1>.
- 714 37. D.Y. Peng, and D. B. Robinson, A new two-constant equation of state, *Ind. Eng. Chem. Fundam.* (1976), 15, 59–64,  
715 <https://doi.org/10.1021/i160057a011>.
- 716 38. G. Soave. Equilibrium constants from a modified Redlich-Kwong equation of state. *Chemical Engineering Science*,  
717 27(6):1197–1203, 1972. ISSN 00092509. doi: 10.1016/0009-2509(72)80096-4.
- 718 39. G. M. Kontogeorgis, E. C. Voutsas, I. V. Yakoumis, and D. P. Tassios. An Equation of State for Associating Fluids.  
719 *Industrial Engineering Chemistry Research*, (11):4310–4318, 1996. ISSN 0888-5885. doi: 10.1021/ie9600203.
- 720 40. H. Gaballa, S. Jafari, A. Di-Lella, CH. Habchi, and J.C De Hemptinne, A tabulated real fluid modeling approach  
721 applied to renewable dual-fuel evaporation and mixing, *ICLASS* (2021), <https://doi.org/10.2218/iclass.2021.5952>.
- 722 41. K.J., P.K. Senecal, and E. Pomraning, 2021. CONVERGE 3.0, Convergent Science, Madison, WI,  
723 <https://convergecf.com>.
- 724 42. F. Nicoud, H.B. Toda, O. Cabrit, S. Bose, and J. Lee, Using singular values to build a subgrid-scale model for large  
725 eddy simulations, *Phys. Fluids* (2011), 23(8), 085106, <https://doi.org/10.1063/1.3623274>.
- 726 43. P. Sagaut, *Large-Eddy Simulation for Incompressible Flows*, 3rd edn. Scientific Computation, 2005, Springer, Berlin  
727 Heidelberg New York, ISBN: 978-3-642-06580-4.
- 728 44. Z. Han, and R.D. Reitz, Turbulence Modeling of Internal Combustion Engines Using RNG k-ε Models, *Combustion*  
729 *Science and Technology* (1995), 106(4-6), 267-295, <https://doi.org/10.1080/00102209508907782>.
- 730 45. P. Yi, S. Jafari, S. Yang, and C. Habchi, “Numerical analysis of subcritical evaporation and transcritical mixing of  
731 droplet using a tabulated multicomponent vapor-liquid equilibrium model, *ILASS–Europe* (2019), 29th Conference  
732 on Liquid Atomization and Spray Systems, <https://ilass19.sciencesconf.org/234493>.
- 733 46. J.-C. de Hemptinne, J.-M. Ledanois, P. Mougouin, and A. Barreau. Select Thermodynamic Models for Process  
734 Simulation - A Practical Guide using a Three Steps Methodology. Technip, 2012. ISBN 9782901638131. [https://doi:](https://doi:10.2516/ifpen/2011001)  
735 10.2516/ifpen/2011001.
- 736 47. C. A. Passut and R. P. Danner. Correlation of Ideal Gas Enthalpy, Heat Capacity and Entropy. *Industrial En-*  
737 *gineering Chemistry Process Design and Development*, 11(4):543–546, 1972. ISSN 0196-4305. [https://doi:](https://doi:10.1021/i260044a016)  
738 10.1021/i260044a016.
- 739 48. T.H Chung, M. Ajlan, L.L. Lee, K.E. Starling, Generalized multi-parameter correlation for non-polar and  
740 polar fluid transport properties, *Industrial and Engineering Chemistry Research* (1988), 27(4): 671–679,  
741 <https://doi.org/10.1021/ie00076a024>.

- 742 49. C. M. Rhie, and W. L. Chow, Numerical Study of the Turbulent Flow Past an Airfoil with Trailing Edge Separation,  
743 AIAA J. (1983), 21, 1525-1532, <https://doi.org/10.2514/3.8284>.
- 744 50. R.I. Issa, A.D. Gosman, and A.P. Watkins, The Computation of Compressible and Incompressible Recirculating Flows  
745 by a Non-Iterative Implicit Scheme, J. of Comput Phys (1986), 62, 66-82, [https://doi.org/10.1016/0021-9991\(86\)90100-](https://doi.org/10.1016/0021-9991(86)90100-2)  
746 2.
- 747 51. P. Linstrom, and W. Mallard, The NIST Chemistry WebBook: A Chemical Data Resource on the Internet, J. Chem.  
748 Eng. Data (2001), vol. 46, no. 5, pp, 1059–1063, <https://doi.org/10.1021/je000236i>.
- 749 52. C. Ware, W. Knight, and D. Wells, Memory intensive statistical algorithms for multibeam bathymetric data, Computers  
750 and Geosciences (1991), vol. 17, no. 7, pp. 985–993, [https://doi.org/10.1016/0098-3004\(91\)90093-S](https://doi.org/10.1016/0098-3004(91)90093-S).
- 751 53. G. Eliosa-Jimenez, G. Silva-Oliver, F. Garcia-Sanchez, A. de Ita de la Torre, High-pressure vapor-liquid equilibria in  
752 the nitrogen + n-hexane system, J. Chem. Eng. (2007), Data 52, 395(404), <https://doi.org/10.1021/je060341d>.
- 753 54. X. Luo, B. Prast, M.E.H. van Dongen, H.W.M. Hoeijmakers, J. Yang: On phase transition in compressible flows:  
754 modelling and validation, J. Fluid Mech, (2006), 548, 403–430
- 755 55. L. Qiu, and R.D. Reitz, An investigation of thermodynamic states during high-pressure fuel in-  
756 jection using equilibrium thermodynamics, J. Multiphas. Flow (2015), Volume 72, Pages 24-38,  
757 <https://doi.org/10.1016/j.ijmultiphaseflow.2015.01.011>.
- 758 56. A. Misdariis, A. Robert, O. Vermorel, S. Richard, T. Poinot, Numerical methods and turbulence modeling for LES  
759 of piston engines: impact on flow motion and combustion, Oil Gas Sci Technol IFP (2013), 69(1), pp. 83-105,  
760 <https://doi.org/10.2516/ogst/2013121>.
- 761 57. M. Rieth, F. Proch, O. Stein, M. Pettit, A. Kempf. Comparison of the sigma and Smagorinsky les models  
762 for grid generated turbulence and a channel flow. Computers and Fluids (2014); 99(Supplement C):172–81,  
763 <https://doi.org/10.1016/j.compfluid.2014.04.018>.
- 764 58. A. Poormahmood, M. Mahdi Salehi, and M. Farshchi, "A methodology for modeling the interaction between turbulence  
765 and non-linearity of the equation of state", Physics of Fluids 34, 015106 (2022) <https://doi.org/10.1063/5.0076099>
- 766 59. P. Chassaing, R. A. Antonia, F. Anselmet, L. Joly, and S. Sarkar, Variable Density Fluid Turbulence, 1st ed.  
767 Springer(2002), <https://doi.org/10.1007/978-94-017-0075-7>.
- 768 60. M.M. Rogers, and R. D. Moser, The three-dimensional evolution of a plane mixing layer: The Kelvin-Helmholtz  
769 rollup, Journal of Fluid Mechanics (2017), 243, 183-226. <https://doi.org/10.1017/S0022112092002696>.
- 770 61. A. Poormahmood, M. Farshchi, Numerical study of the mixing dynamics of trans- and supercritical coaxial jets. Phys.  
771 Fluids (2020), 32, 125105, <https://doi.org/10.1063/5.0030183>.
- 772 62. S. Baab, C. Steinhäuser, G. Lamanna, B. Weigand, and F.J. Förster, A quantitative speed of sound database for  
773 multicomponent jet mixing at high pressure, Fuel (2018), 233:918–925, <https://doi.org/10.1016/J.FUEL.2017.12.080>.
- 774 63. L. Davidson, and M. Billson, Hybrid LES-RANS using synthesized turbulent fluctuations for forcing in the interface  
775 region, International Journal of Heat and Fluid Flow, 27, 1028-1042, 2006. DOI: 10.1016/j.ijheatfluidflow.2006.02.025.
- 776 64. J.M. Desantes, J.M. García-Oliver, J.M. Pastor, I. Olmeda, A. Pandal, B. Naud, LES Eulerian diffuse-interface  
777 modeling of fuel dense sprays near- and far-field, International Journal of Multiphase Flow, 2020, 103272, ISSN  
778 0301-9322, <https://doi.org/10.1016/j.ijmultiphaseflow.2020.103>.
- 779 65. J.M. Desantes, J.M. García-Oliver, J.M. Pastor, A. Pandal, B. Naud, K. Matusik, D. Duke, A. Kastengren, C. Powell,  
780 D.P. Schmidt, Modelling and valida- tion of near-field Diesel spray CFD simulations based on the –Ymodel. In:  
781 Proceedings of the 28th European Conference on Liquid Atomization and Spray Systems, September 6–8, Valencia,  
782 Spain, 2017, doi: 10.4995/ILASS2017.2017.4715.
- 783 66. A. B. Wood, A Textbook of Sound. Third Edition. Bell, London, 1955. 610 pp. Illustrated. 42s, (1957), The Journal  
784 of the Royal Aeronautical Society, 61(554), 138-138, <https://doi.org/10.1017/S0368393100130998>.